Role of Runoff–Infiltration Partitioning and Resolved Overland Flow on Land–Atmosphere Feedbacks: A Case Study with the WRF-Hydro Coupled Modeling System for West Africa

JOEL ARNAULT AND SVEN WAGNER

Institute of Meteorology and Climate Research, Karlsruhe Institute of Technology, Garmisch-Partenkirchen, and Chair for Regional Climate and Hydrology, Institute of Geography, University of Augsburg, Augsburg, Germany

THOMAS RUMMLER

Chair for Regional Climate and Hydrology, Institute of Geography, University of Augsburg, Augsburg, Germany

BENJAMIN FERSCH

Institute of Meteorology and Climate Research, Karlsruhe Institute of Technology, Garmisch-Partenkirchen, Germany

JAN BLIEFERNICHT AND SABINE ANDRESEN

Chair for Regional Climate and Hydrology, Institute of Geography, University of Augsburg, Augsburg, Germany

HARALD KUNSTMANN

Institute of Meteorology and Climate Research, Karlsruhe Institute of Technology, Garmisch-Partenkirchen, and Chair for Regional Climate and Hydrology, Institute of Geography, University of Augsburg, Augsburg, Germany

(Manuscript received 28 May 2015, in final form 28 September 2015)

ABSTRACT

The analysis of land–atmosphere feedbacks requires detailed representation of land processes in atmospheric models. The focus here is on runoff–infiltration partitioning and resolved overland flow. In the standard version of WRF, runoff–infiltration partitioning is described as a purely vertical process. In WRF-Hydro, runoff is enhanced with lateral water flows. The study region is the Sissili catchment ($12\,800\,\text{km}^2$) in West Africa, and the study period is from March 2003 to February 2004. The WRF setup here includes an outer and inner domain at 10- and 2-km resolution covering the West Africa and Sissili regions, respectively. In this WRF-Hydro setup, the inner domain is coupled with a subgrid at 500-m resolution to compute overland and river flow. Model results are compared with TRMM precipitation, model tree ensemble (MTE) evapotranspiration, Climate Change Initiative (CCI) soil moisture, CRU temperature, and streamflow observation. The role of runoff–infiltration partitioning and resolved overland flow on land–atmosphere feedbacks is addressed with a sensitivity analysis of WRF results to the runoff–infiltration partitioning parameter and a comparison between WRF and WRF-Hydro results, respectively. In the outer domain, precipitation is sensitive to runoff–infiltration partitioning at the scale of the Sissili area ($\sim100 \times 100\,\text{km}^2$), but not of area A ($500 \times 2500\,\text{km}^2$). In the inner domain, where precipitation patterns are mainly prescribed by lateral boundary conditions, sensitivity is small, but additionally resolved overland flow here clearly increases infiltration and evapotranspiration at the beginning of the wet season when soils are still dry. The WRF-Hydro setup presented here shows potential for joint atmospheric and terrestrial water balance studies and reproduces observed daily discharge with a Nash–Sutcliffe model efficiency coefficient of 0.43.

---

1. Introduction

The atmosphere is influenced by the land surface, but the precise mechanisms by which land–atmosphere feedbacks occur are not fully understood yet (e.g., Seneviratne et al. 2006; Adler et al. 2011; Santanello et al. 2013; Koster et al. 2014). In particular, the role of soil moisture and vegetation on air temperature and precipitation is a subject of debate (e.g., Pielke 2001; Koster et al. 2004, 2006; Guo et al. 2006; Dirmeyer 2011). As recalled by Guo et al. (2006), strong soil moisture–precipitation feedbacks require a robust coupling of surface evapotranspiration (ET) to soil wetness (i.e., the terrestrial segment), as well as a strong link between precipitation and surface fluxes through convection (i.e., the atmospheric segment). Concerning the terrestrial segment of soil moisture–precipitation feedbacks, soil moisture has been found to be the main controlling factor for ET in transition zones between wet and dry areas, where soil moisture–limited ET regimes prevail (Koster et al. 2004; Dirmeyer 2011), eventually resulting in soil moisture–induced thermal circulations (e.g., Pielke 2001; Taylor et al. 2007, 2011a). This is particularly the case for the West African region situated between the wet Guinean coast and the dry Saharan desert, where rainfall strongly influences the spatial distribution of soil moisture and surface fluxes (Taylor et al. 2007, 2011a,b). Based on surface–atmosphere exchange measurements acquired during field experiments of the African Monsoon Multidisciplinary Analyses (AMMA; Redelsperger et al. 2006; Lebel et al. 2009; Peugeot et al. 2011), Schwendike et al. (2010) and Lohou et al. (2014) found a larger response of ET to soil moisture disturbances at the beginning of the monsoon when soils are still dry (Kunstmann and Jung 2007; Yamada et al. 2013). Concerning the atmospheric segment of soil moisture–precipitation feedbacks, the role of soil moisture–induced thermal circulations on convective development finally depends on the state of the atmosphere, and in particular on the amount of convective available potential energy (CAPE), convective inhibition (CIN), and winds (e.g., Pielke 2001; Findell and Eltahir 2003; Taylor et al. 2007, 2011a,b; van den Hurk and van Meijgaard 2010; Gantner and Kalthoff 2010; Froidevaux et al. 2014). For example, in West Africa, testing different soil moisture initializations in a numerical simulation of mesoscale convective systems (MCSs), Gantner and Kalthoff (2010) obtained a decrease of rainfall for a mature MCS when approaching dry soils, although the convergent anomaly above such dry soils also favored convection initiation. A comprehensive analysis of the life cycle of organized convection in West Africa was given by Laing et al. (2008).

The potential influence of the land surface on the atmosphere raises the question of whether a more detailed representation of land processes in numerical atmospheric models, for example, vegetation dynamics and terrestrial hydrology, would significantly affect model results (e.g., Delire et al. 2011; Stéfanon et al. 2012; Maxwell et al. 2007, 2011; Anyah et al. 2008; Jung et al. 2010; Koster et al. 2010; Shrestha et al. 2014; Larsen et al. 2014). Maxwell et al. (2007) coupled the Advanced Regional Prediction System (ARPS; Xue et al. 2000) with ParFlow, a three-dimensional and variably saturated groundwater flow model (PF.ARPS; Jones and Woodward 2001), for an idealized case study of convective initiation in a 600-km^2 watershed in Oklahoma, United States. Numerical experiments at 1-km horizontal resolution with PF.ARPS and ARPS stand-alone were conducted for a 36-h period. The PF.ARPS simulation additionally used 390 soil layers with a spacing of 0.5 m for resolving subsurface water flows in the full aquifer depth. Maxwell et al. (2007) found significant differences in the location of convective cells at the end of the 36-h run between the two simulations, in association with shallow water-table depths in the valley in the PF.ARPS simulation and a strong sensitivity of surface fluxes to soil moisture disturbances (i.e., soil moisture–limited ET regime). The Regional Atmospheric Modeling System (RAMS; Walko et al. 2000) was enhanced with a groundwater reservoir, a dynamic water table–river exchange, and river flow routing to the ocean (RAMS-Hydro; Miguez-Macho et al. 2007). Anyah et al. (2008) performed a 6-month RAMS-Hydro simulation in May–October 1997 for the whole United States, using horizontal resolutions of 50 and 12.5 km for the atmospheric and hydrologic components of the model, respectively. In comparison to a RAMS stand-alone simulation, it was found that water table–induced wetter soils in RAMS-Hydro increased ET in the western regions of the United States, where soil moisture was a strong limiting factor for ET (as in Maxwell et al. 2007), but did not have much influence in the more humid eastern regions of the United States, where soil moisture was not limiting in general. The increase of ET in the RAMS-Hydro simulation was further associated with an increase of precipitation through local recycling. Shrestha et al. (2014) coupled the Consortium for Small-Scale Modeling (COSMO) system (Schättler et al. 2008) and ParFlow within the Terrestrial Systems Modeling Platform (TerrSysMP). A 1-week TerrSysMP simulation in July 2012 was performed for the 2300 km^2 Rur catchment in Germany, at horizontal resolutions of 1 and 0.5 km for the COSMO and ParFlow components of the model, respectively. Also, 30 stretched layers down to 30 m below the surface were used for the terrestrial

vertical grid. Model results were significantly sensitive to soil moisture disturbances (i.e., soil moisture–limited ET regime; Maxwell et al. 2007; Anyah et al. 2008). Moreover, in comparison to COSMO stand-alone, TerrSysMP-resolved surface fluxes were generally closer to observations.

The Weather Research and Forecasting (WRF) Model (Skamarock and Klemp 2008) was recently coupled with the National Center for Atmospheric Research (NCAR) Distributed Hydrologic Modeling System (NDHMS) within the so-called WRF-Hydro modeling system (Gochis and Chen 2003; Gochis et al. 2014). In the WRF standard version, coupled with the Noah land surface model (LSM; Chen and Dudhia 2001), runoff–infiltration partitioning is computed in a 2-m soil column without taking into account lateral water flow. In WRF-Hydro, the Noah LSM is enhanced with overland and river flow routing via NDHMS, thus accounting for horizontal processes involved in runoff–infiltration partitioning. Also, subsurface routing in the saturated zone of the 2-m soil column and a groundwater bucket model for evaluating the contribution of base flow to river discharge are possible, but not activated in this study. Similarly to RAMS-Hydro (e.g., Anyah et al. 2008), WRF-Hydro does not solve the three-dimensional subsurface water flows, which makes it more computationally suitable for investigating the role of a physically enhanced description of terrestrial hydrology on land–atmosphere feedbacks in a multimonth simulation, as compared to TerrSysMP (Shrestha et al. 2014).

Modifying or improving the land surface representation (e.g., WRF-Hydro vs WRF) in a coupled land–atmosphere simulation of the West African region is expected to significantly affect the simulated West African monsoon system (e.g., Steiner et al. 2009; Hagos et al. 2014). Moufouma-Okia and Rowell (2009) found that varying soil moisture initial condition in a regional climate simulation for West Africa generates small random intraseasonal and interannual spatial variations in simulated precipitation. In their case, modifying lateral boundary conditions had a larger impact in terms of magnitude and spatial coherency. However, as claimed by Agustí-Panareda et al. (2010), the full value of additional land surface information may improve the accuracy of a numerical simulation only if the basic atmospheric processes involved in the West African monsoon system are already adequately captured. The West African monsoon, that is, the latitudinal displacement of the tropical rain belt over West Africa, is indeed the result of a complex scale interaction process involving sea surface temperature fluctuations, land surface characteristics, oceanic monsoon flow, Saharan Heat Low (SHL), African Easterly Jet (AEJ), African

Easterly Wave (AEW), Tropical Easterly Jet (TEJ), and MCSs [see the comprehensive review of Nicholson (2013)].

In a 5-yr simulation at 50-km resolution with the International Centre for Theoretical Physics (ICTP) Regional Climate Model, version 3 (RegCM3; Pal et al. 2007), driven by ERA-Interim (Dee et al. 2011), Browne and Sylla (2012) showed that modeled West African summer rainfall is sensitive to the size of the simulated domain used for resolving atmospheric processes at stake. Simulated rainfall characteristics closest to those from the Tropical Rainfall Measuring Mission (TRMM; Huffman et al. 2007) dataset were obtained for a domain including a large portion of the Atlantic Ocean in the south (10°S) and regions upstream of the Sudanese highlands to the east (35°E), as it allowed the regional atmospheric model to develop a sufficiently moist oceanic monsoon flow and to generate its own AEW disturbances with respect to the driving data, respectively. The ability of a numerical simulation to correctly represent atmospheric processes involved in the West African monsoon system also depends on the choice of model physics. For example, simulating the West African monsoon in April–September 1999 with a WRF domain at 24-km resolution and 27 different configurations of physical parameterization, Klein et al. (2015) obtained a spread in Sahelian precipitation in August as large as that observed for a 30-yr period (1979–2010). Simulating the West African monsoon for a 10-day period at a resolution of 12 km, Marsham et al. (2013) compared the impact of parameterized and explicit convection on model results. In their case, explicit convection gave the closest rainfall amount and diurnal timing with respect to TRMM precipitation data. It also gave more realistic monsoon dynamics as deduced by a simulated meridional surface pressure gradient closer to ground observation. The model configuration without cumulus parameterization was therefore considered as the most suitable for a future coupled application with other components of the Earth system in West Africa, such as hydrology in our case.

The West African region situated between the wet Guinean coast and the dry Saharan desert can be divided in a Sahelian subregion, northward of the 700-mm isohyet, and a Sudanian subregion southward [following Descroix et al. (2009)]. The location of this 700-mm isohyet is at approximately 12°–14°N. As recalled by Descroix et al. (2009), the main hydrological difference between the Sahelian and Sudanian ecoclimates is the amount of rainfall: generally less than 700 mm in the Sahelian case and between 700 and 1300 mm in the Sudanian case. In the Sahelian region, hillslope runoff is usually generated through Hortonian overland flow

occurring during a rainfall event when infiltration capacity is reached (e.g., Dunne 1978; Casenave and Valentin 1992; Peugeot et al. 1997; Esteves and Lapetite 2003). Furthermore, there is observational evidence that infiltration potentially occurs at the bottom of Sahelian river beds (Peugeot et al. 1997). In the Sudanian region, soil infiltration capacity is generally higher because of more vegetated areas, tillage, faunal activity, and less soil crusting, so that in this case subsurface hydrological processes play a larger role in surface runoff generation (e.g., Casenave and Valentin 1992; Chevallier and Planchon 1993). Accordingly, depths to groundwater in this region are found to vary between 0 and 25 m (Bonsor and Mac Donald 2011).

Distributed hydrological models generally do not describe the full complexity of surface runoff generation processes, but they can be calibrated for the purpose of discharge estimation in large-scale river basins, as was shown by Wagner et al. (2006) and d'Orgeval and Polcher (2008) for several West African river basins. Forcing the Water Flow and Balance Simulation Model (WaSiM; Schulla and Jasper 2007) with outputs from the Fifth-generation Pennsylvania State University–NCAR Mesoscale Model (MM5; Grell et al. 1994), Wagner et al. (2006) and Jung et al. (2012) showed the potential of coupled atmospheric–hydrological modeling in estimating river discharges in the White Volta basin, a river basin situated between southern Burkina Faso and northern Ghana, in between the Sudanian and Sahelian regions. The main problem in forcing such hydrological models with atmospheric model data, however, remains the limited accuracy of simulated precipitation (e.g., Smiatek et al. 2012).

The additional description of terrestrial lateral water flows in coupled atmospheric–hydrological models potentially affects simulation results in regions characterized by soil moisture–limited ET regimes (e.g., Maxwell et al. 2007; Anyah et al. 2008; Shrestha et al. 2014). However, such coupled models have never been applied to the West African region, although numerous studies have shown the impact of soil moisture on surface fluxes and precipitation there (e.g., Kunstmann and Jung 2007; Taylor et al. 2007, 2011a,b; Gantner and Kalthoff 2010; Schwendike et al. 2010; Yamada et al. 2013; Lohou et al. 2014). Consequently, the present work aims at evaluating the performance of the WRF-Hydro coupled modeling system for the West African environment in reproducing hydrometeorological datasets. The primary objective of this study is to assess the impact of runoff–infiltration and overland flow on land–atmosphere feedbacks in WRF and WRF-Hydro simulations. The secondary objective is to evaluate the ability of WRF-Hydro to model the full atmospheric–hydrological

regional water cycle and to reproduce finally observed streamflow. Such a model skill would indeed be particularly relevant for West Africa, a region threatened by droughts and characterized by a primarily rainfed agriculture (Nicholson 2000).

Our study focuses on the Sissili catchment ($\sim$12 800 km^2, 10.2°–12°N, 1°–2.5°W; see Fig. 1), a subbasin of the White Volta basin and a core research site of the West African Science Service Center on Climate Change and Adapted Land Use (WASCAL; Bliefernicht et al. 2013). The period of investigation is from March 2003 to February 2004. This choice has been motivated by 1) the low anthropogenic influence in the Sissili catchment compared to other West African river basins due to the absence of dams and the presence of a nature reserve in its northern part (the Nazinga Reserve), 2) the comprehensiveness of investigating a hydrological year from one dry season to the next one, and 3) the rare simultaneous availability of daily discharge time series at the outlet of the Sissili catchment (Wiasi gauge location displayed in Fig. 1c) and further meteorological datasets in this region (see section 2). It is noted here that the Sissili catchment is situated in a part of the West African Sudanian region where both overland flow and subsurface hydrological processes are expected to contribute to surface runoff generation [see Fig. 2 of Descroix et al. (2009)]. In the following, the region surrounding the Sissili catchment is referred to as the West African Sudano-Sahelian region.

Section 2 presents the observational datasets used in this study to describe the atmospheric–hydrological conditions of the Sissili catchment and surrounding Sudano-Sahelian region from March 2003 to February 2004. The WRF and WRF-Hydro setups are described in section 3. The methodology to investigate the role of runoff–infiltration partitioning and resolved overland flow on modeled land–atmosphere feedbacks is detailed in section 4. Results are provided in section 5. Conclusions and perspectives of this work are given in section 6.

2. Observational datasets

Atmospheric–hydrological characteristics of the Sissili catchment and surrounding Sudano-Sahelian region for the 12-month period from March 2003 to February 2004 are investigated here with four global observational datasets of precipitation P, soil moisture volumetric content θ, evapotranspiration, and near-surface temperature T, and with Sissili streamflow observation at Wiasi Q_{Wiasi} (Wiasi gauge location displayed in Fig. 1c).

The P dataset comes from TRMM (P_{TRMM}; Huffman et al. 2007), the θ dataset from the Climate Change Initiative (CCI) of the European Space Agency (ESA;
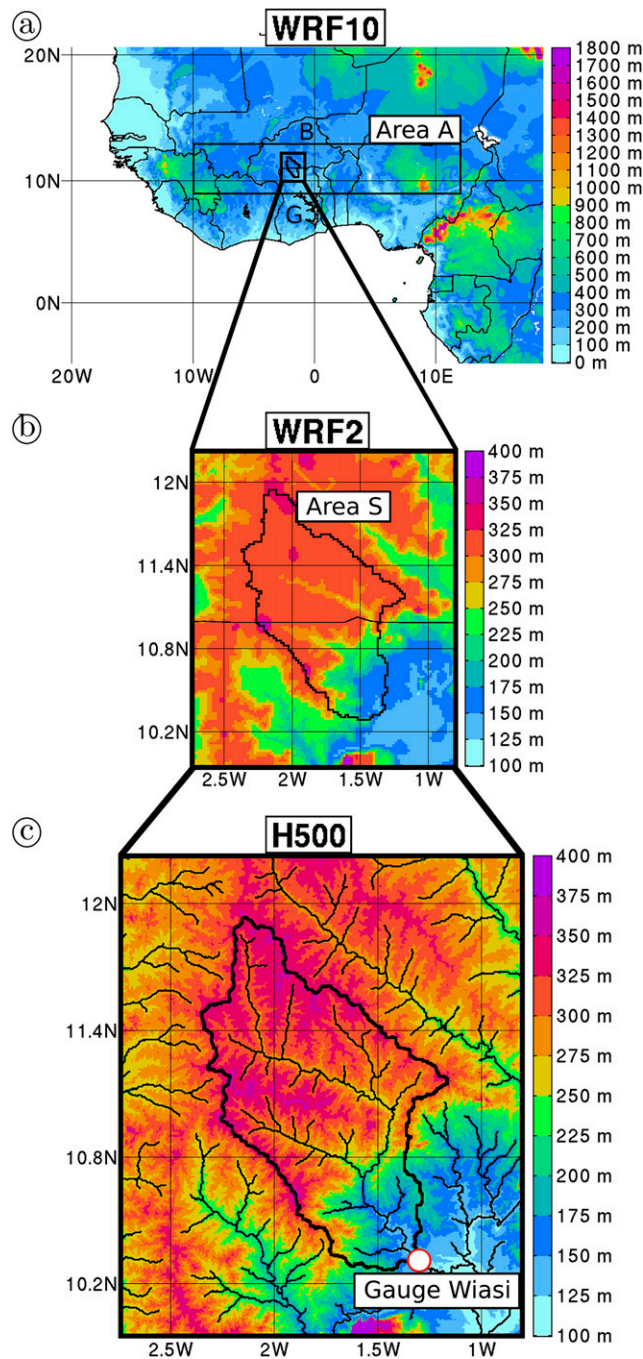
FIG. 1. (a) Terrain elevation (m MSL) of WRF10. The height scale is given by the colored bar to the right. The curved black lines delineate the West African coast and the political boundaries. Burkina Faso and Ghana are indicated by labels ''B'' and ''G,'' respectively. The thick black rectangle shows the location of the nested domain displayed in (b), and the black closed contour inside this rectangle delineates the area of the Sissili catchment. The east–west elongated rectangle delineates area A. (b) Terrain elevation (m MSL) of WRF2. The height scale is given by the colored bar to the right. The black closed contour inside this rectangle delineates the area of the Sissili catchment (labeled ''Area S''). (c) Terrain elevation (m MSL) of H500 coupled with WRFH2. The black lines show river channels with a Strahler stream order above 3. The position of Wiasi gauge is also indicated.

θ_{CCI}; Dorigo et al. 2014), the ET dataset from the model tree ensemble (MTE; ET_{MTE}; Jung et al. 2009, 2010), the T dataset from the Climatic Research Unit (CRU; T_{CRU}; Harris et al. 2014), and the Q_{Wiasi} dataset from the Hydrological Services Department of the Ministry of Water Resources, Works and Housing of Ghana. The P_{TRMM} and θ_{CCI} have a spatial resolution of 0.25° and are provided 3-hourly and daily, respectively, whereas ET_{MTE} and T_{CRU} have a spatial resolution of 0.5° and are monthly products. The P_{TRMM} is commonly used for evaluating West African precipitation (e.g., Nicholson et al. 2003; Browne and Sylla 2012; Marsham et al. 2013; Klein et al. 2015). Comparing P_{TRMM} with interpolated gauge measurements in the Volta basin in West Africa, Thiemig et al. (2012) found that P_{TRMM} could be used to accurately estimate yearly amounts and monthly variation of precipitation. On the daily scale, however, P_{TRMM} showed discrepancies with respect to the number of rainy days and the magnitude of heavy rainfall events. Nevertheless, P_{TRMM} was found to be one of the most accurate satellite-based rainfall products for the West African region (Thiemig et al. 2012). The ET_{MTE} has been chosen with respect to two other available ET datasets from the Moderate Resolution Imaging Spectroradiometer (MODIS) Global Evapotranspiration Project (MOD16; Mu et al. 2007, 2011), and from Global Land Surface Evaporation: The Amsterdam Methodology (GLEAM; Miralles et al. 2011). As highlighted by Lorenz et al. (2014), each of these gridded products performs differently for different river basins. The best agreement between our WRF results and these ET datasets was found with ET_{MTE} (not shown here).

To facilitate comparison with model outputs (section 4), P_{TRMM}, θ_{CCI}, ET_{MTE}, and T_{CRU} datasets are interpolated on the WRF grid at 10-km resolution (Fig. 1a) using the nearest-neighbor interpolation technique. The Q_{Wiasi} is displayed as specific discharge (volumetric discharge divided by the area of the Sissili catchment) in order to provide an estimation of surface runoff R in the Sissili catchment in the same units (i.e., $mm\,day^{-1}$) as the other observed hydrological fluxes involved in the surface water budget.

Monthly time series of P_{TRMM}, ET_{MTE}, θ_{CCI}, and T_{CRU}, spatially averaged for the Sissili catchment area, as well as monthly time series of Q_{Wiasi}, are displayed in Fig. 2 (see thick lines). A wet period occurred in the Sissili region from March to October 2003, followed by a dry period from November 2003 to February 2004 (Fig. 2b). The Q_{Wiasi} mainly followed the distribution of P_{TRMM}, with a single peak in September and near-zero values at the beginning of the wet period and during the dry months (Fig. 2a). This unimodal behavior is a typical feature of river discharge usually observed in the region

(e.g., Wagner et al. 2006). There was almost no baseflow contribution during the dry season, although this does not exclude a contribution of subsurface hydrological processes to the generation of Q_{Wiasi} during wet months (e.g., Chevallier and Planchon 1993). For T_{CRU}, two distinct peaks occurred during the considered 12-month period, one in April and another in October, at the beginning and end of the wet period, respectively (Fig. 2e). The comparatively lower T_{CRU} between May and September was associated with comparatively higher θ_{CCI} and ET_{MTE} (cf. Figs. 2c–e), confirming a strong soil moisture–temperature feedbacks in this West African region during the wet period (e.g., Koster et al. 2006; Taylor et al. 2007). According to these observations, the amount of precipitation from March 2003 to February 2004 in the Sissili catchment was 1199 mm, in association with 737 mm of ET and 72 mm of discharge (see second row of Table 1). This gives an annual runoff ratio of 6.1%.

It is stressed that global gridded products (P_{TRMM}, θ_{CCI}, ET_{MTE}, and T_{CRU}) are based on remote sensing data and a limited number of ground observations, so that discrepancies in the water balance can be expected when looking at a relatively small area such as the Sissili catchment ($\sim 100 \times 100\,km^2$). To mitigate this resolution issue, we spatially average these products for the much larger area A defined as 9°–13°N, 10°W–12°E (location displayed in Fig. 1a; see thick lines in Fig. 3). A comparison between Fig. 2 and Fig. 3 shows that the monthly variations of spatially averaged P_{TRMM}, ET_{MTE}, θ_{CCI}, and T_{CRU} in the Sissili catchment and area A are similar. Even the annual amounts of precipitation and ET are close (cf. second row of Tables 1 and 2). This suggests that atmospheric–hydrological characteristics of the Sissili catchment are typical for the surrounding Sudano-Sahelian region defined as area A. However, runoff ratios cannot be compared since no discharge data are available for the whole area A. It is noted here that surface runoff in area A is an area-averaged variable that can, on the other hand, be deduced from model outputs (see Fig. 3a, Table 2).

Given the temporal resolution of P_{TRMM}, that is, 3-hourly, the Sissili catchment and area A are further characterized with mean diurnal cycles and daily histograms (see thick lines in Fig. 4). The mean diurnal cycles are computed with 3-hourly P_{TRMM} spatially averaged in the considered area (Sissili catchment or area A) for the period April–October 2003. The daily histograms are computed with daily P_{TRMM} averaged in $50 \times 50\,km^2$ subareas within the considered area and for the same time period. Mean diurnal cycles show a precipitation peak around 1800 UTC for both Sissili catchment and area A, which is a known feature of West
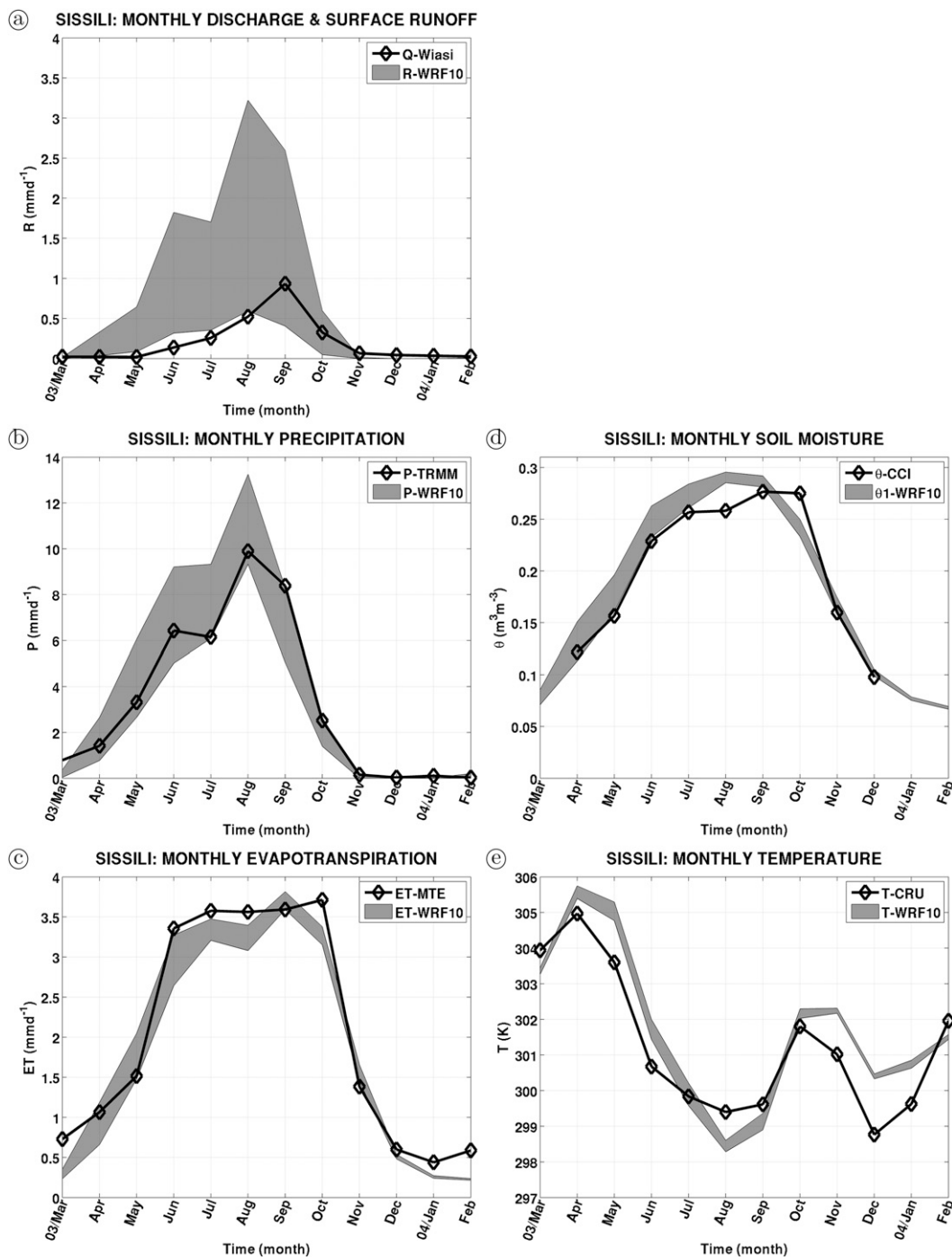
FIG. 2. Monthly time series of the observed atmospheric–hydrological variables spatially averaged in the area of the Sissili catchment (black solid lines with diamond): (a) Q_{Wiasi} (mm day^{-1}), (b) P_{TRMM} (mm day^{-1}), (c) ET$_{\text{MTE}}$ (mm day^{-1}), (d) θ_{CCI} (m^3 m^{-3}), and (e) T_{CRU} (K). The computation of area-averaged monthly θ_{CCI} in (d) is in two steps: 1) monthly averaged values of θ_{CCI} are deduced from the mean of daily area-averaged values of θ_{CCI} available at each pixel of the dataset, and 2) when the number of pixels with available monthly θ_{CCI} in the area of the Sissili catchment is greater than 20%, then an area-averaged monthly θ_{CCI} is computed. The gray range in each panel comes from the seven WRF10 simulations' results with $k = 3, 6, 9, 12, 15, 18$, and 21. The x axis gives the time in months from March 2003 to February 2004, and the y axis gives the scale of the displayed quantity.

TABLE 1. Annual characteristics of the observed atmospheric–hydrological variables in the area of the Sissili catchment for the 1-yr period from March 2003 to February 2004: Q_{Wiasi} (Q and R) and P_{TRMM} (P), runoff ratio between Q_{Wiasi} and P_{TRMM}, amount of ET_{MTE} (ET), mean of θ_{CCI} for the period of available data (θ), and mean of T_{CRU} (T). Rows denote the differences between each of the seven WRF10 simulations' results with k = 3, 6, 9, 12, 15, 18, and 21, and observations. Note that annual amounts of R_{WRF10} are compared with the annual amount of Q_{Wiasi} in the first column. Data from columns P, ET, θ, and T are displayed in Fig. 6a.

	Q and R (mm)	P (mm)	Runoff ratio (%)	ET (mm)	θ (m^3 m^{-3})	T (K)
Obs	73 mm	1199	6.1	737	0.203	301.27
WRF10, k = 3	+261	+165	24.5	−55	+0.014	+0.43
WRF10, k = 6	+111	+64	14.6	−43	+0.013	+0.48
WRF10, k = 9	+61	+37	10.9	−55	+0.010	+0.46
WRF10, k = 12	+44	+53	9.4	−85	+0.006	+0.41
WRF10, k = 15	+30	+126	7.8	−40	+0.015	+0.36
WRF10, k = 18	−2	−7	6.0	−53	+0.013	+0.35
WRF10, k = 21	−14	−38	5.2	−62	+0.010	+0.42

African precipitation (e.g., Laing et al. 2008). The afternoon peak in the case of area A is, however, less pronounced, in association with the large meridional span covered by area A, that is, 10°W–12°E (cf. Figs. 4a,c). Histograms of daily precipitation in the Sissili catchment and area A are also similar. In particular, between April and October 2003, 50 × 50 km^2 subareas within these two regions received on average less than 1 mm of daily precipitation 52%–53% of the time, 1–5 (5–20, 20–40) mm of daily precipitation 17%–19% (21%–22%, 6%–7%) of the time, and more than 40 mm of daily precipitation about 1% of the time (see Figs. 4b,d).

In the following, we assess to which extent these atmospheric–hydrological observations can be reproduced by standard WRF using a single-column land surface model compared to WRF-Hydro.

3. Models

a. WRF Model: Description and setup for West Africa

A two-domain WRF setup is considered in this study, an outer domain at 10-km resolution encompassing most of the West African continent (Fig. 1a) and a nested inner domain at 2-km resolution covering a 240 × 280 km^2 area around the Sissili catchment (Fig. 1b), using a one-way nesting technique. In the following, the outer domain is referred to as WRF10 and the inner domain as WRF2. WRF10 consists of a Mercator-projected domain covering a sufficiently large area to the south (5°S) and to the east (20°E), in order to resolve the oceanic monsoon flow and AEW disturbances (Browne and Sylla 2012). In both WRF10 and WRF2 the vertical grid consists of 35 vertical levels up to 20 hPa (~25 km), with a vertical spacing stretched from 70 to 1000 m at the lowest and highest levels, respectively. The simulated period is 14 months from January 2003 to February 2004, thereby including a 2-month spinup time

(see section 5a). The initial and lateral boundary conditions of WRF10 are from the 0.75°-resolution ERA-Interim (Dee et al. 2011). The model equations in WRF10 and WRF2 are integrated at a time step of 50 and 10 s, respectively, and outputs are saved at an hourly interval.

It has to be noted that the recommendations of Browne and Sylla (2012) are not strictly respected here, as WRF10 does not extend as far south (i.e., 10°S) and as far east (i.e., 35°E) as suggested. This smaller domain size was chosen in order to reduce computing time while keeping the 10-km resolution. Indeed, as shown in the following analysis, this resolution appears to be sufficient to simulate West African 3-hourly, daily, and monthly rainfall characteristics comparable to those derived from TRMM data without cumulus parameterization (as in Marsham et al. 2013). Test simulations with the Kain–Fritsch cumulus scheme (Kain 2004; Ma and Tan 2009) enabled in WRF10 have also been considered. The main difference was an increase of the overestimation of weak precipitation events and annual precipitation amounts in the study region by about 10% (with respect to TRMM data) when the cumulus scheme was enabled (not shown). The configuration without cumulus scheme in WRF10 was therefore retained in this study.

WRF10 and WRF2 use the same parameterized physics. Microphysics is parameterized with the five-class liquid and ice hydrometeors scheme of Hong et al. (2004). Radiative processes are represented with the longwave and shortwave radiation schemes of Mlawer et al. (1997) and Dudhia (1989), respectively. Turbulent transport of heat, moisture, and momentum is parameterized in the whole atmospheric column with the scheme of Hong et al. (2006). Surface exchange coefficients are computed according to Chen and Zhang (2009) in order to take into account the effect of canopy height on land–atmosphere exchanges. Surface heat and
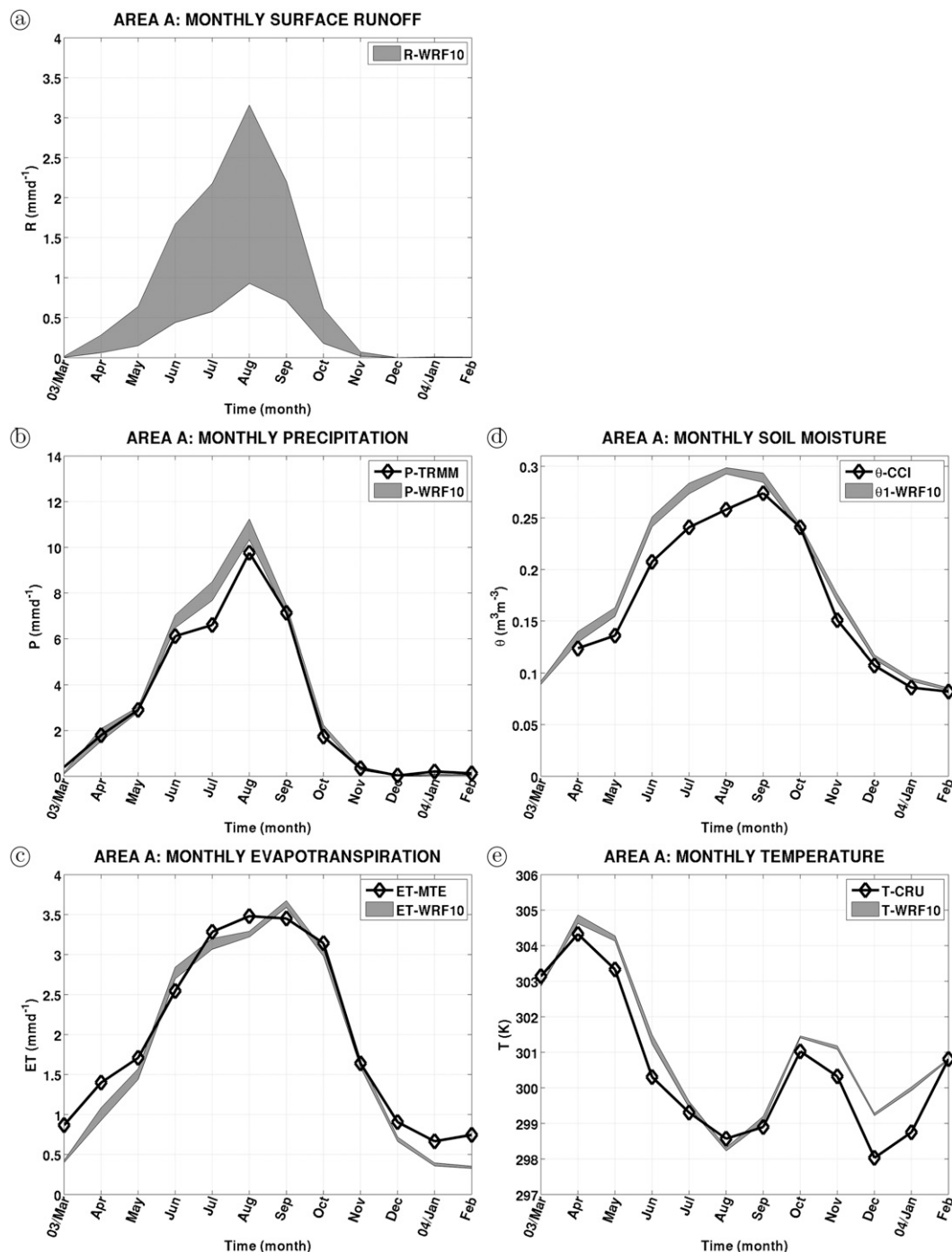
FIG. 3. As in Fig. 2, but for area *A* shown in Fig. 1a. Also, no discharge observation is displayed in (a) because these data are not available for area *A*.

moisture fluxes are calculated, with the one-dimensional Noah LSM predicting soil temperature and soil moisture in a 2-m-depth, four-layer column and taking into account vegetation effects (Chen and Dudhia 2001). Land surface parameters used in the Noah LSM, such as stomatal resistance, roughness length, and canopy height,

are assigned for each category of the land-use map. Land use is deduced from the MODIS land-cover map (Friedl et al. 2002) using the dominant-category criteria for the interpolation to the WRF domain's resolution. Albedo, green vegetation fraction, and leaf area index (LAI), three other important parameters in the Noah LSM, are

TABLE 2. As in Table 1, but for area A. Note that the first column indicates the annual amount of R_{WRF10} since there is no discharge observation for area A. Data from columns P, ET, θ, and T are displayed in Fig. 6b.

	R (mm)	P (mm)	Runoff ratio (%)	ET (mm)	θ (m^3 m^{-3})	T (K)
Obs	—	1137	—	728	0.173	300.57
WRF10, $k = 3$	332	+101	26.8	−78	+0.015	+0.53
WRF10, $k = 6$	229	+95	18.6	−67	+0.018	+0.51
WRF10, $k = 9$	175	+84	14.3	−64	+0.017	+0.53
WRF10, $k = 12$	149	+108	12.0	−62	+0.019	+0.47
WRF10, $k = 15$	123	+89	10.1	−56	+0.020	+0.48
WRF10, $k = 18$	109	+95	8.8	−50	+0.021	+0.47
WRF10, $k = 21$	94	+82	7.7	−55	+0.020	+0.48

taken from satellite-derived climatology (Csiszar and Gutman 1999; Gutman and Ignatov 1998; Kumar et al. 2014).

b. The bare soil evaporation parameter fx in Noah LSM

The single-column Noah LSM computes the moisture flux from the nonvegetated fraction of a model grid box, that is, bare soil evaporation E_{dir} (m s^{-1}), as

$$E_{dir} = (1 - \sigma_f)\left(\frac{\theta_1 - \theta_{dry}}{\theta_{sat} - \theta_{dry}}\right)^{fx}(E_p), \qquad (1)$$

where P_d (m) is the precipitation not intercepted by the canopy; ΔZ_i (m) is the depth of soil layer i; θ_i is the volumetric water contents (soil moisture) in soil layer i; θ_s is the saturated soil moisture (porosity), which depends on soil texture; K_s (m s^{-1}) is the saturated hydraulic conductivity, which also depends on soil texture; $K_{ref} = 2 \times 10^{-6}$ m s^{-1} depicts the saturated hydraulic conductivity of the silty–clay–loam soil texture chosen as a reference; δ_t (s) is the model time step; and k is the runoff–infiltration partitioning parameter [k stands for kdt$_{ref}$ in Chen and Dudhia (2001)]. Indeed, in Eq. (2) k regulates the rate of surface infiltration at each time step, taking into account the volume of rainfall water at the surface and the potential volume of water that can still be contained in the 2-m soil layer until saturation, so that surface runoff (infiltration) can be decreased (increased) by increasing k (Schaake et al. 1996). Time integrating Eq. (2) gives a measure of modeled surface

where σ_f is the green vegetation fraction; θ_1 (m^3 m^{-3}) is the volumetric soil water content in the first Noah soil layer between 0 and 10 cm; θ_{dry} (m^3 m^{-3}) and θ_{sat} (m^3 m^{-3}) are the minimal and saturated values, respectively; E_p (m s^{-1}) is the potential evaporation; and fx is the bare soil evaporation parameter (Ek et al. 2003). This parameter affects the declining rate of soil moisture, bare soil evaporation, and its default value is set to 2.

c. The runoff–infiltration partitioning parameter k in Noah LSM

The single-column Noah LSM computes the change in surface water depth h (m) as the rate of infiltration excess (Chen and Dudhia 2001):

$$\frac{\partial h}{\partial t} = \frac{\partial P_d}{\partial t}\left\{1 - \frac{\left[\sum_{i=1}^{4}\Delta Z_i(\theta_s - \theta_i)\right]\left[1 - \exp\left(-k\frac{K_s}{K_{ref}}\frac{\delta_t}{86\,400}\right)\right]}{P_d + \left[\sum_{i=1}^{4}\Delta Z_i(\theta_s - \theta_i)\right]\left[1 - \exp\left(-k\frac{K_s}{K_{ref}}\frac{\delta_t}{86\,400}\right)\right]}\right\}, \qquad (2)$$

runoff, that is, R_{WRF10} and R_{WRF2} for the outer and inner domain, respectively, which is saved in the outputs.

In the case of a river basin where surface infiltration excess is mainly responsible for surface runoff generation, spatially averaged R_{WRF10} and R_{WRF2} in the river basin provide an estimation of river specific discharge, which can then be calibrated by tuning k. Based on field experiments (Wood et al. 1998), the default value of k has been set to 3, although Chen and Dudhia (2001) recognized that this parameter should be calibrated again for basins with different precipitation climatology.

d. Description of the hydrological module for the WRF-Hydro setup

The WRF-Hydro setup considered here is based on the WRF setup described in section 3a. Additionally, the inner domain (Fig. 1b) is coupled with a routing subgrid
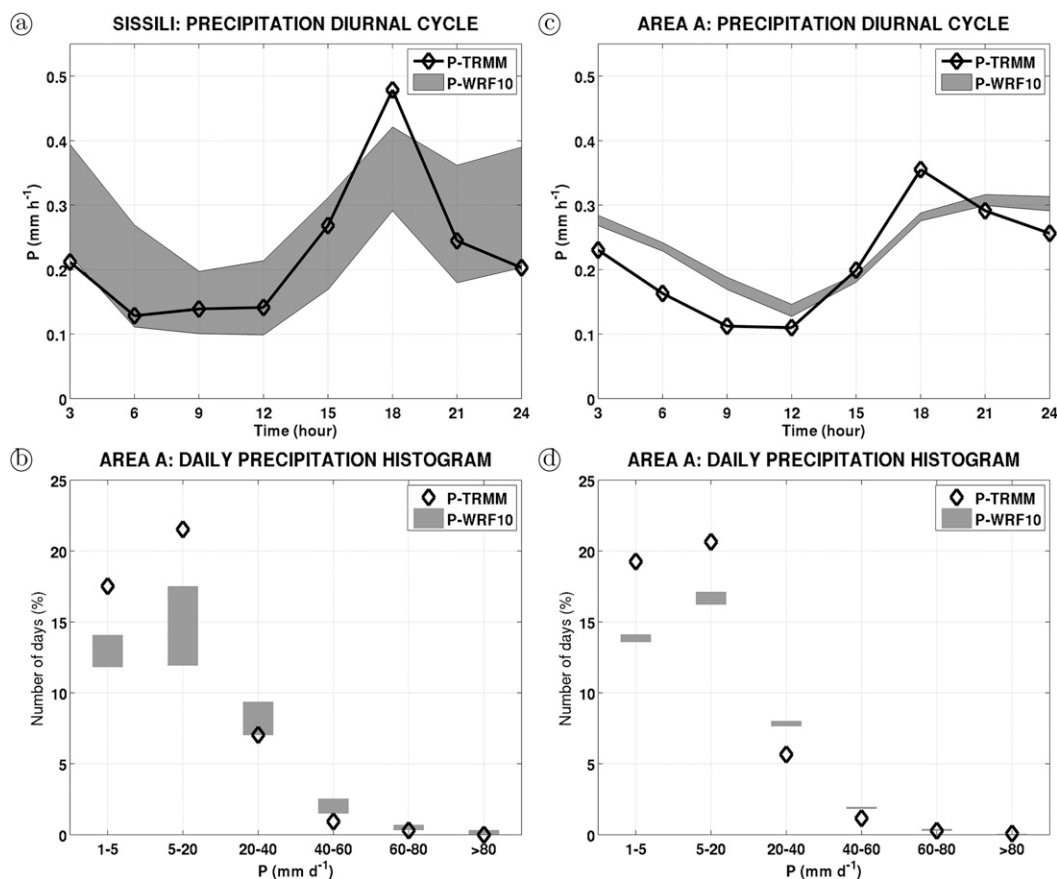
FIG. 4. (a) Mean diurnal cycle of the Sissili catchment–averaged precipitation (mm h^{-1}) derived from TRMM data (black solid line with diamonds) and from the WRF10 simulations with k = 3, 6, 9, 12, 15, 18, and 21 (gray range) for the period April–October 2003. The x axis gives the time of the day (h UTC), and the y axis gives the precipitation scale (mm h^{-1}). (b) The histogram of daily precipitation (mm day^{-1}) averaged in 50×50 km^2 subareas within in the area of the Sissili catchment. The x axis gives precipitation bins (mm day^{-1}), and the y axis gives the amount of days (%). (c),(d) As in (a),(b), but for area A.

at 500-m resolution (Fig. 1c) for the computation of overland and streamflow routing. In the following, the inner domain of the WRF-Hydro setup is referred to as WRFH2 and the routing grid as H500.

The H500 is obtained with the WRF-Hydro preprocessing tool, taking as input data the digital elevation data (DEM) from the Hydrological Data and Maps Based on Shuttle Elevation Derivatives at Multiple Scales (HydroSHEDS) database (Lehner et al. 2008). It provides elevation, surface flow direction, and the river network displayed in Fig. 1c, obtained by setting the minimal number of pixels to define a stream to four in the preprocessing tool. This means that the minimal resolved catchment area in H500 is 1 km^2 (i.e., 4 $\times$ 500 m $\times$ 500 m). This minimal number leads to a density of stream grid cells of about 26% for the whole routing grid. It is noted here that the choice of this minimal number is arbitrary. Test simulations using higher

minimal numbers, that is, less dense river network, gave lower discharge (not shown).

Overland flow routing is computed on H500 at the WRFH2 time resolution in two steps. First, the rate of infiltration excess h determined by the one-dimensional Noah land surface model in WRFH2 [see Eq. (2)], considered here as the rate of surface flow depth, is disaggregated on H500 using linear subgrid weighting factors. Second, overland flow, occurring when h exceeds a specified retention depth, is solved on H500 with a diffusive wave formulation adapted from Julien et al. (1995) and Ogden (1997), using Manning's surface roughness coefficients from Vieux (2001).

Streamflow routing is computed on the river network of H500 (Fig. 1c) also at the WRFH2 time resolution, but with an additional variable time-stepping technique in order to satisfy Courant constraints. This computation is done in two steps. First, the discharge of overland flow

TABLE 3. Channel parameters as a function of Strahler stream order. The channel bottom width b_w, side slope $\tan\alpha$, initial river head h_{init}, and default Manning's channel roughness coefficients n are from the ''Noah test case'' for WRF-Hydro (available online at http://www.ral.ucar.edu/projects/wrf_hydro). The calibrated Manning's coefficients used in this work are indicated in the last column.

Strahler stream order	b_w (m)	$\tan\alpha$	h_{init} (m)	n default	n calibrated
1	1.5	3.0	0.02	0.55	0.75
2	3.0	1.0	0.02	0.35	0.70
3	5.0	0.5	0.02	0.15	0.65
4	10.0	0.18	0.03	0.10	0.60
5	20.0	0.05	0.03	0.07	0.55
6	40.0	0.05	0.03	0.05	0.30
7	60.0	0.05	0.03	0.04	0.20

into a stream, the so-called lateral flow q_{lat} (m^3 s^{-1}), is computed as

$$q_{lat} = \frac{\partial h}{\partial t} \times a_{cgrid}, \qquad (3)$$

where t (s) is the time coordinate and a_{cgrid} (m^2) is the area of a channel grid cell in $H500$. Second, the water volume within the river network is routed on a pixel-by-pixel basis using a diffusive wave formulation allowing for backwater effects. Channel parameters, including the initial river head, bottom width, and side slope of the river channel, as well as Manning's channel roughness coefficient, are prescribed as functions of Strahler stream order (Strahler 1957). Default values are provided in Table 3 [further details can be found in Gochis et al. (2014)].

For each model time step, after the computation of overland and streamflow routing on $H500$, the remaining surface flow depth h is aggregated to WRFH2 using the same linear subgrid weighting factors used for the disaggregation. Aggregated surface flow depth is then added to precipitation not intercepted by the canopy [term P_d in Eq. (2)] for computation of soil moisture infiltration at the next model time step, thus including feedbacks of surface lateral water flows in WRFH2. It is noted here that q_{lat} [Eq. (3)] gives the rate of surface water in $H500$ that does not infiltrate in the ground but reaches the river network instead, so that this quantity is directly related to the surface runoff predicted by WRF-Hydro (i.e., R_{WRFH2}). The aggregation and temporal integration of q_{lat} on WRFH2 have been implemented in the code and added to the model outputs, in order to provide a measure of R_{WRFH2} comparable to the surface runoff predicted in the WRF inner domain stand-alone, that is, R_{WRF2}.

4. Methodology of feedback analysis

It is recalled that land–atmosphere feedbacks refer to the two-way interaction between terrestrial and atmospheric variables, such as soil moisture, surface runoff, evapotranspiration, surface temperature, and precipitation (e.g., Seneviratne et al. 2010; Koster et al. 2014). WRF and WRF-Hydro are physically based models that resolve the processes governing these variables, at least partially. A method to evaluate the role of a particular process on land–atmosphere feedbacks is to compare two WRF/WRF-Hydro simulations in which the description of this process is modified. The relevance of the result from such a sensitivity analysis can then be assessed against 1) observation and 2) model uncertainty obtained from an ensemble analysis (e.g., Hagos et al. 2014).

The focus here is on runoff–infiltration partitioning and overland flow, two processes taken into account in the Noah LSM of WRF [Eq. (2)] and in the hydrological extension of WRF-Hydro [Eq. (3)], respectively. Model results for the outer, inner, and hydrologically enhanced inner domain, that is, WRF10, WRF2, and WRFH2, respectively, are evaluated with observational datasets presented in section 2. Recognizing that soil moisture initial condition may affect the role of runoff–infiltration partitioning on soil moisture and potential land–atmosphere feedbacks, the significance of spinup for land surface conditions is investigated in section 5a for WRF10. The role of runoff–infiltration partitioning on land–atmosphere feedbacks is assessed in section 5b with a sensitivity analysis of WRF10 results to the runoff–infiltration partitioning parameter k [Eq. (2)]. For this purpose, the model setup of section 3a, including WRF10 only, is run seven times with values of $k = 3, 6, 9, 12, 15, 18,$ and 21. Scale effects are considered by analyzing feedbacks in the Sissili catchment and in the surrounding West African Sudano-Sahelian region, that is, area A (Fig. 1a). In section 5c, the significance of the role of runoff–infiltration partitioning on modeled land–atmosphere feedbacks deduced from the sensitivity analysis of WRF10 results to k is assessed against an ensemble of seven additional WRF10 simulations in which the soil moisture initial condition is varied. The ensemble of soil moisture initial conditions is constructed with the seven soil moisture fields at 0000 UTC 1 January 2004 derived from the WRF10 simulations with varied values of k. It is assumed here that simulated soil moisture conditions at 0000 UTC 1 January 2004, after a 1-yr simulation run, are plausible conditions for a model initialization at 0000 UTC 1 January 2003.

A sensitivity analysis of WRF2 results to k is provided in section 5d. The model setup of section 3a, with both
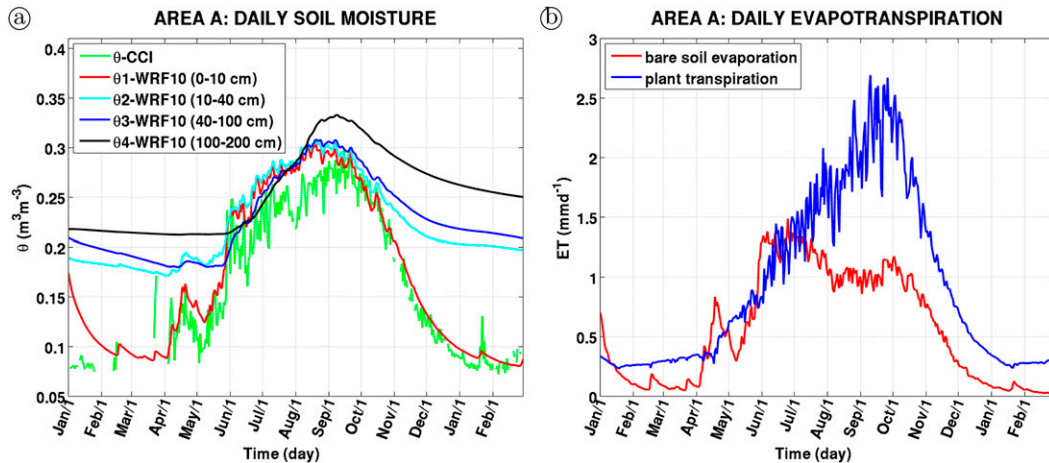
FIG. 5. (a) Area A–averaged daily soil moisture from CCI (θ_{CCI}) and from the four Noah LSM soil layers of the WRF10 simulation with $k = 3$ ($\theta_{i\text{-WRF10}}$; $i = 1, 4$). The x axis gives the time from 1 Jan 2003 to 28 Feb 2004, and the y axis gives the θ scale (m³ m⁻³). (b) As in (a), but for the area A–averaged daily bare soil evaporation and plant transpiration (mm day⁻¹) from the same WRF10 simulation.

WRF10 and WRF2, is run with the default value of k and with the value of k that gives the WRF10 results closest to observations. It is noted that the WRF code has been upgraded in order to specify k separately for the outer and inner domain, so that the sensitivity of WRF2 results to k is tested separately. This allows investigating the role of runoff–infiltration partitioning on land–atmosphere feedbacks in the Sissili catchment at a higher resolution and in the theoretical case of fixed large-scale conditions (one-way nesting).

In WRF-Hydro, the description of runoff–infiltration partitioning [Eq. (2)] is enhanced with resolved overland flow [Eq. (3)]. It is therefore expected that WRF-Hydro and WRF have different sensitivity to k. Calibration issues with WRF-Hydro are addressed in section 5e. The dependency of land–atmosphere feedbacks to resolved overland flow is finally investigated by comparing WRF2 and WRFH2 calibrated results (section 5f).

5. Results

a. Significance of spinup for land surface conditions

Figure 5a shows the daily averaged θ_{CCI} and soil moisture in the four soil layers of the WRF10 simulation with $k = 3$ ($\theta_{i\text{-WRF10}}$; $i = 1, 4$) for the area A. Note that θ_{CCI} is compared here with $\theta_{1\text{-WRF10}}$, the volumetric soil water content in the first Noah soil layer between 0 and 10 cm [the validity of such a comparison was suggested by Albergel et al. (2008), Brocca et al. (2011), and Dorigo et al. (2014)]. Daily area A–averaged bare soil evaporation and plant transpiration from the WRF10 simulation are also displayed in Fig. 5b. The $\theta_{1\text{-WRF10}}$

and bare soil evaporation are relatively high at the beginning of the simulation but display a sharp decrease during the first simulated month. This suggests that there is an excess of $\theta_{1\text{-WRF10}}$ in area A at the initial time of the simulation, which is drained out through bare soil evaporation during the first simulated month. Then, the amounts of $\theta_{1\text{-WRF10}}$ and bare soil evaporation at the end of February 2003 are close to those reached at the end of February 2004. Also, $\theta_{1\text{-WRF10}}$ and θ_{CCI} are close in February 2003 and 2004. Therefore, in this particular case, a 2-month spinup period appears to be sufficient for soil moisture in the first soil layer.

Plant transpiration, on the other hand, shows a much weaker dependency on the relatively high initial $\theta_{1\text{-WRF10}}$ (see Fig. 5b). It is also noticeable that θ in deeper layers, between 10 and 200 cm depth, is significantly higher at the end of the simulation as compared to 12 months earlier (about 10% more between 10 and 100 cm, and 17% more between 100 and 200 cm; Fig. 5a), so that a 2-month period may not be fully sufficient for modeled θ in deeper layers to spin up. A multiyear simulated time period for deep θ spinup time (e.g., Santanello et al. 2013) would certainly affect plant transpiration, infiltration capacity, runoff–infiltration partitioning, and ultimately land–atmosphere feedbacks.

b. Sensitivity of outer domain results to runoff–infiltration partitioning

To test the effect of runoff–infiltration partitioning on WRF10 results, seven simulations are conducted for the WRF outer domain with values of $k = 3, 6, 9, 12, 15, 18,$ and 21 [see Eq. (2)]. As expected, k has a large impact on modeled monthly surface runoff (R_{WRF10}) in the area of
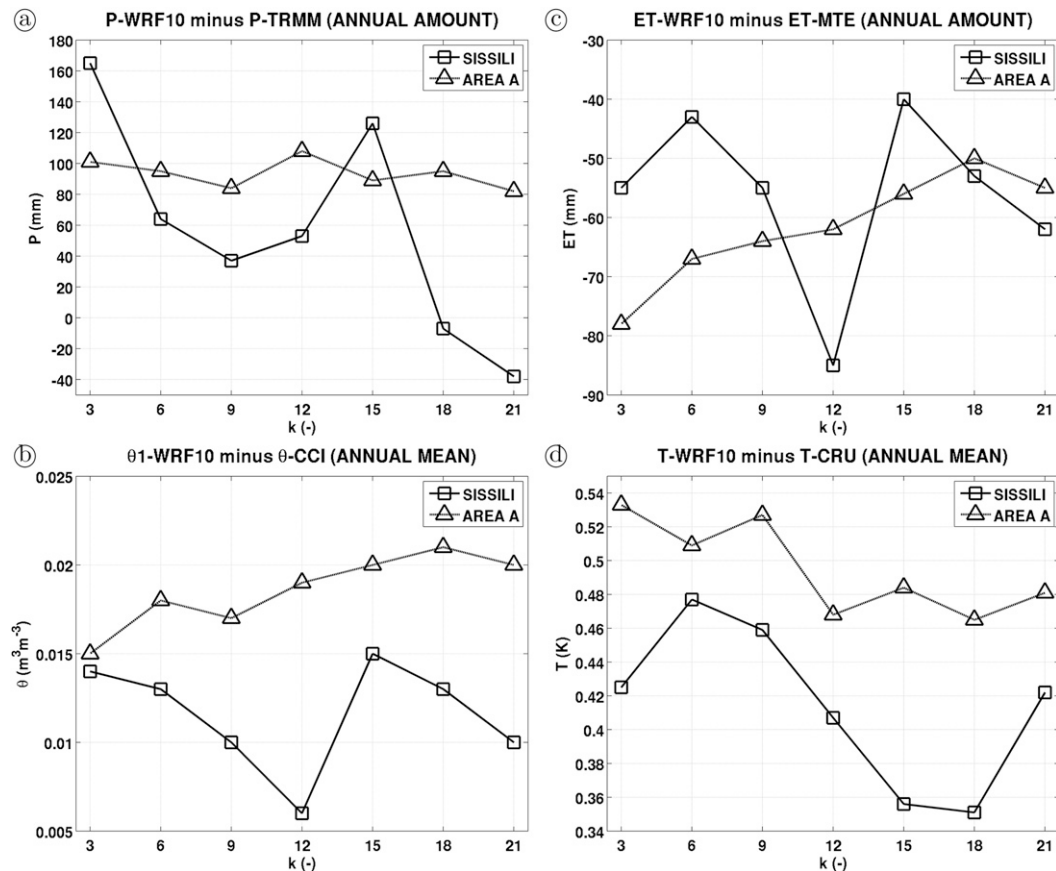
FIG. 6. (a) Difference between the annual amount of P_{WRF10} and P_{TRMM} for the period from March 2003 to February 2004 in the area of the Sissili catchment (black line with squares) and in area A (dashed line with triangles), as a function of k. The x axis gives the value of the k parameter and the y axis gives the P (mm). (b) As in (a), but for the difference between the annual mean of $\theta_{1\text{-WRF}}$ and θ_{CCI}. The x axis gives the value of the k parameter and the y axis gives the θ (m^3 m^{-3}). (c) As in (a), but for the difference between the annual mean of ET_{WRF} and ET_{MTE}. The x axis gives the value of the k parameter and the y axis gives the ET (mm). (d) As in (a), but for the difference between the annual mean of T_{WRF} and T_{CRU}. The x axis gives the value of the k parameter and the y axis gives the T (K).

the Sissili catchment (see Fig. 2a). In consequence, k also has an impact on other simulated monthly atmospheric–hydrological characteristics of the Sissili catchment, that is, P_{WRF10}, ET_{WRF10}, $\theta_{1\text{-WRF10}}$, and T_{WRF10} (see gray range in Figs. 2b–e, respectively). Annual differences between model results and observations for the 1-yr period from March 2003 to February 2004 are provided in Table 1 and Fig. 6. Modeled annual surface runoff in the Sissili catchment, that is, R_{WRF10}, is compared with observed annual discharge at the outlet Wiasi, that is, Q_{Wiasi}, which is justified by the fact that these annual quantities are computed between a dry season and the next one, that is, a hydrological year. Variations in k lead to variations in the range of 275 and 203 mm for the annual amount of R_{WRF10} and P_{WRF10}, respectively, which corresponds to 377% and 17% of the annual amounts of observed R_{Wiasi} and P_{TRMM}, respectively

(Table 1). On the one hand, the difference between annual amounts of R_{WRF10} and Q_{Wiasi} decreases with increasing k; on the other hand, such a linear behavior with respect to k does not exist for the difference of annual amounts between P_{WRF10} and P_{TRMM} and ET_{WRF10} and ET_{MTE}, nor does it exist for the difference of annual mean between θ_{WRF10} and θ_{CCI} and T_{WRF10} and T_{CRU} (see lines with squares in Fig. 6).

There is a larger variability of monthly $\theta_{1\text{-WRF10}}$ and ET_{WRF10} with respect to k from April to July (see Figs. 2c,d), confirming a larger response of surface fluxes to soil moisture disturbances at the beginning of the monsoon (Kunstmann and Jung 2007; Schwendike et al. 2010; Yamada et al. 2013; Lohou et al. 2014). In August, for all k, ET_{WRF10} and T_{WRF10} are lower than ET_{MTE} and T_{CRU}, respectively, whereas $\theta_{1\text{-WRF10}}$ is higher than $\theta_{1\text{-CCI}}$. These results are obtained for the default value of

2 for the bare soil evaporation parameter [see section 3c, Eq. (1)]. A test simulation with fx = 1 (not shown here) confirmed that decreasing fx increases (decreases) bare soil evaporation and ET_{WRF10} ($\theta_{1\text{-}WRF10}$ and T_{WRF10}). Since T_{WRF10} in August is already lower than T_{CRU}, the beneficial impact of decreasing fx for ET_{WRF10} and $\theta_{1\text{-}WRF10}$ in August is therefore mitigated. This apparent inconsistency between model and observations could be due to the fact that other model parameters impacting T_{WRF10}, such as surface albedo, are not properly prescribed. Also, ET_{WRF10} is systematically lower than ET_{MTE} at the beginning of the wet season (March) and during dry months (December–February). The relatively higher ET_{MTE} during these dry months could be related to the presence of deep-rooted vegetation in the West African Sudano-Sahelian region (e.g., Schenk and Jackson 2005), since this is not taken into account in the 2-m-depth soil thickness of Noah LSM. However, the present work does not aim at improving the description of ET_{WRF10}, but at quantifying the impact of runoff–infiltration calibration on ET_{WRF10} and other variables characterizing modeled land–atmosphere feedbacks. All evapotranspiration parameters in the Noah LSM, including fx, are therefore kept to their default value in the present study.

It is, however, difficult to judge which value of k gives the most accurate WRF10 results in the Sissili catchment, since k = 18, 18, 15, 12, and 18 give the smallest annual difference among R_{WRF10}, P_{WRF10}, ET_{WRF10}, θ_{WRF10}, and T_{WRF10} and respective observations. This highlights the difficulty of capturing the complicated soil moisture–precipitation feedback mechanisms occurring in the Sissili catchment (e.g., Kunstmann and Jung 2007; Gantner and Kalthoff 2010). It is remarkable that k = 18 provides the closest annual amount of precipitation and surface runoff with respect to observation (see Table 1), with an annual runoff ratio of 6%. It is therefore suggested that physically realistic values of k can be much higher than the maximum value of 10 assumed by Santanello et al. (2013), depending on the study region.

The effect of runoff–infiltration partitioning on WRF10 results at the scale of the West African Sudano-Sahelian region, that is, area A, is investigated in Figs. 3 and 6 and Table 2. It is noticeable that at this scale, the diminution of surface runoff, that is, increase of k, results in an overall slight increase of θ_{WRF10} and ET_{WRF10} (see dashed lines with triangles in Figs. 6b,c). There is also an overall slight decrease of T_{WRF10} between k = 3 and 21, although this decrease is clearly nonlinear with respect to k (see dashed line with triangle in Fig. 6d). Variations in P_{WRF10} are also nonlinear (see dashed line with triangles in Fig. 6a). The impact of k on P_{WRF10}, ET_{WRF10}, θ_{WRF10}, and T_{WRF10} for area A is, however, rather small in comparison to differences with observations. The

TABLE 4. RMSE (mm h^{-1}) between the WRF10- and TRMM-derived precipitation diurnal cycles displayed in Figs. 4a and 4d for the Sissili catchment and area A.

	Sissili catchment	Area A
WRF10, k = 3	0.21	0.16
WRF10, k = 6	0.29	0.16
WRF10, k = 9	0.17	0.15
WRF10, k = 12	0.30	0.16
WRF10, k = 15	0.29	0.15
WRF10, k = 18	0.24	0.16
WRF10, k = 21	0.23	0.15

lower impact of k on precipitation at the scale of area A, as compared to that at the scale of the Sissili catchment (see Fig. 6a), would facilitate the calibration of this parameter at this scale, although discharge data are not available for the whole area A. Moreover, for such a large area, there is certainly a need to spatially distribute k in order to account for the full variability in soil and surface properties. Nevertheless, an annual runoff ratio of 8.8% in area A is obtained for the WRF10 simulation using k = 18, which is of the same order of magnitude as that obtained for the Sissili catchment (6%).

The mean diurnal cycles and daily histograms of P_{TRMM} and P_{WRF10} displayed in Fig. 4 show a large (small) variability of 3-hourly and daily P_{WRF10} with respect to k at the scale of the Sissili catchment (area A). The mean diurnal cycle in the Sissili catchment closest to that from TRMM, with respect to RMSE, is obtained with k = 9 (Table 4). For the daily histogram of Fig. 4b, however, there is no k tested value that systematically provides the closest percentage of days for a given precipitation bin as that derived from TRMM (not shown). The correlation coefficient between area A–averaged (Sissili catchment averaged) daily time series of P_{WRF10} and P_{TRMM} varies between 0.64 and 0.70 (0.16 and 0.31), depending on the k tested value (see second line of Table 5). This means that WRF10 performs better in simulating accurate daily precipitation at the scale of area A than at the scale of the Sissili catchment. Moreover, daily time series of area A–averaged P_{WRF10} are much more correlated between themselves in comparison to daily time series of Sissili catchment–averaged P_{WRF10} (Table 5).

The impact of k on model results is further quantified in Figs. 7 and 8 with time series of so-called spatial correlations of precipitation. Spatial correlation is defined here as the correlation, between two precipitation datasets, of all subarea-averaged precipitation elements within a given area. Figure 7 displays the monthly evolution of spatial correlation of $100 \times 100\,\text{km}^2$ averaged monthly precipitation elements in area A between P_{TRMM} and P_{WRF10}. It shows a large variability of

TABLE 5. Correlation coefficients between each pair of TRMM- and WRF10-derived daily precipitation time series for the period April–November 2003 for the Sissili catchment (italics) and area A (boldface).

	$P_{WRF10}, k = 3$	$P_{WRF10}, k = 6$	$P_{WRF10}, k = 9$	$P_{WRF10}, k = 12$	$P_{WRF10}, k = 15$	$P_{WRF10}, k = 18$	$P_{WRF10}, k = 21$
P_{TRMM}	*0.26*	*0.25*	*0.28*	*0.25*	*0.31*	*0.16*	*0.28*
	0.68	**0.66**	**0.68**	**0.70**	**0.68**	**0.64**	**0.66**
$P_{WRF10}, k = 3$		*0.36*	*0.40*	*0.37*	*0.49*	*0.47*	*0.48*
		0.84	**0.86**	**0.88**	**0.86**	**0.87**	**0.88**
$P_{WRF10}, k = 6$			*0.45*	*0.28*	*0.45*	*0.37*	*0.43*
			0.88	**0.82**	**0.85**	**0.80**	**0.84**
$P_{WRF10}, k = 9$				*0.27*	*0.54*	*0.48*	*0.41*
				0.86	**0.86**	**0.84**	**0.86**
$P_{WRF10}, k = 12$					*0.49*	*0.41*	*0.48*
					0.88	**0.86**	**0.88**
$P_{WRF10}, k = 15$						*0.56*	*0.48*
						0.86	**0.87**
$P_{WRF10}, k = 18$							*0.56*
							0.89

simulated monthly precipitation with respect to k in subareas of a size comparable to that of the Sissili catchment ($\sim$12 800 km^2), although no model configuration is providing monthly precipitation systematically closer to TRMM. Figure 8 displays the distribution of mean spatial correlations of 100×100 km^2 averaged daily precipitation elements in area A, as a function of mean precipitation. These spatial correlations are found between 0.1 and 0.7, which further confirms that k has a significant impact on simulated daily precipitation at the 100-km-scale characteristic of the Sissili catchment.

To summarize, modifying the runoff–infiltration partitioning parameter k for the whole outer domain, in order to get modeled annual surface runoff in the Sissili catchment as close as possible to observed annual discharge, does modify significantly the hourly, daily, monthly, and yearly atmospheric–hydrological characteristics of the Sissili catchment ($\sim$100 $\times$ 100 km^2) and leads to annual precipitation closer to TRMM observation. Also, at the scale of the West African Sudano-Sahelian region (i.e., area A, $\sim$500 $\times$ 2500 km^2), k has a similar impact on surface runoff, but a much reduced influence on other atmospheric–hydrological variables, that is, soil moisture, evapotranspiration, near-surface temperature, and precipitation.

c. Sensitivity of outer domain results to soil moisture initial condition

The significance of the role of runoff–infiltration partitioning on land–atmosphere feedbacks deduced from a sensitivity analysis to k (section 5b) is assessed here against a sensitivity analysis to soil moisture initial condition. A set of seven soil moisture fields at 0000 UTC 1 January 2004 is derived from the previously discussed WRF10 simulations with values of $k = 3, 6, 9, 12, 15, 18,$ and 21. These fields are all different from each

other, in association with the previously described model result variability to k. In particular, the spatial RMSE at pixel scale (10×10 km^2 subareas) in area A between each pair is in the range of 5%–7%. These soil moisture fields are used to initialize seven additional WRF10 simulations at 0000 UTC 1 January 2003 with k fixed to 18.

Results of this sensitivity analysis are displayed in Figs. 9 and 10 for the area of the Sissili catchment and
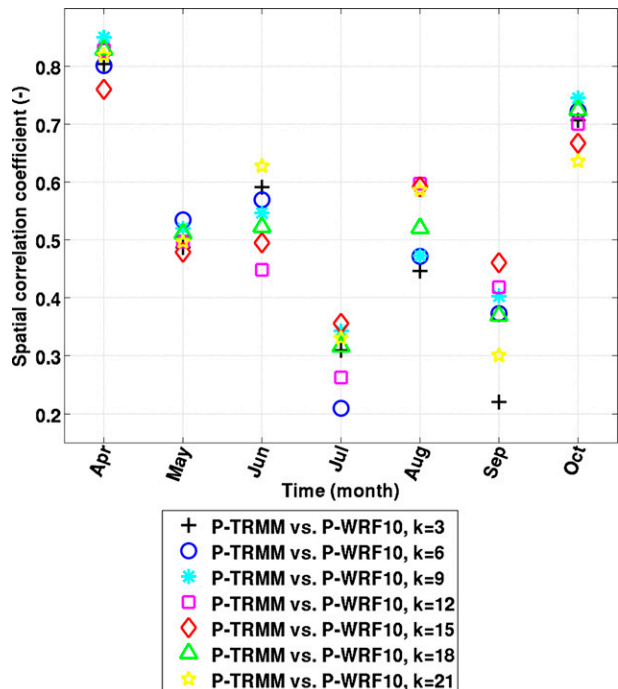
FIG. 7. Spatial correlation between 100×100 km^2 subareas of TRMM monthly precipitation in area A and those from the WRF10 simulations using $k = 3, 6, 9, 12, 15, 18,$ and 21. The x axis gives the time in months from April to October 2003, and the y axis gives the spatial correlation scale.
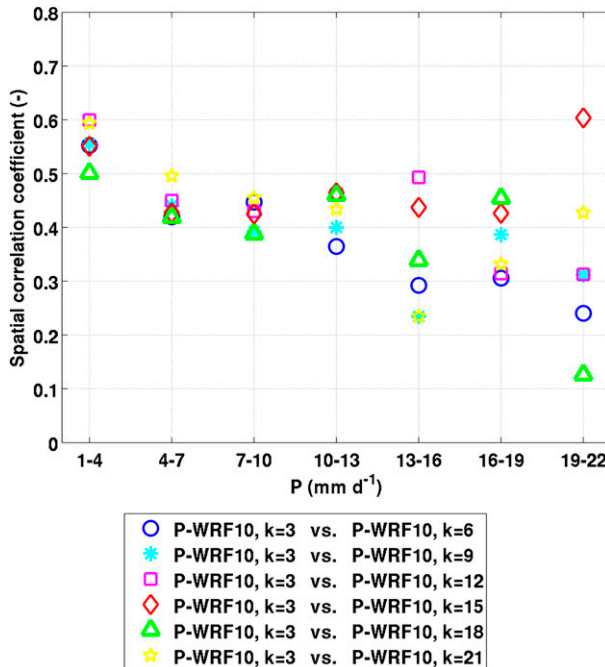
FIG. 8. As in Fig. 7, but for the spatial correlation between daily precipitation from the WRF10 simulation using $k = 3$ and that from the six other WRF10 simulations using $k = 6$, 9, 12, 15, 18, and 21. Also, spatial correlations shown here are averaged for the selected bins of mean daily precipitation in area A and plotted as a function of these bins (see x axis).

area A, respectively. It shows that soil moisture initialization has a significant (much reduced) impact on monthly precipitation, soil moisture, evapotranspiration, and temperature in the Sissili catchment (area A). A similar impact is found for the mean daily cycle and daily histogram of precipitation (not shown). It is remarkable that this model sensitivity to soil moisture initial condition is comparable with that to k (cf. Figs. 2b–e and Figs. 9b–e, Figs. 3b–e and Figs. 10b–e), except for surface runoff (cf. Fig. 2a and Fig. 9a, Fig. 3a and Fig. 10a). Indeed the sensitivity of surface runoff to k is related to precipitation variability and runoff–infiltration partitioning calibration. The sensitivity of surface runoff to soil moisture initial condition is related to precipitation variability only, leading to much smaller surface runoff variability in this case. Model results variability introduced by soil moisture initial condition is further assessed with the distribution of mean spatial correlations of $100 \times 100 \, \text{km}^2$ averaged daily precipitation elements in area A, as a function of mean precipitation (Fig. 11). These spatial correlations are comparable with those obtained in the sensitivity analysis to k, except for high precipitation events where the impact of k is clearly larger (i.e., lower spatial correlations; cf. Figs. 8 and 11 for precipitation bins above $16 \, \text{mm day}^{-1}$).

It is concluded that the role of runoff–infiltration partitioning on West African precipitation is at least as important as that of soil moisture initial condition, which is in accordance with the findings of Moufouma-Okia and Rowell (2009). On the other hand, the previous result that $k = 18$ gives the most accurate annual amount of precipitation (Table 1) is mitigated since this also depends on soil moisture initialization.

d. Sensitivity of inner domain results to runoff–infiltration partitioning

In the case of WRF10 with default soil moisture initialization, it was shown that $k = 18$ gives the most accurate annual amount of surface runoff and precipitation in the Sissili catchment (section 5b, Table 1). It is proposed here to test this calibrated value of k for the one-way nested 2-km inner domain WRF2 on the basis of three WRF simulations using the setup described in section 3a and $k = 3$ and 3, 3 and 18, and 18 and 18, for WRF10 and WRF2, k being specified separately for each domain. It is noted that WRF2 with $k = 3$ and 3 and WRF2 with $k = 3$ and 18 have identical lateral boundary conditions, so that differences between them are only due to WRF2-resolved land–atmosphere feedbacks in response to modified runoff–infiltration partitioning.

Compared to WRF10, WRF2 simulates significantly more surface runoff (cf. second column in Tables 1 and 6). In particular, the difference between annual amounts of R_{WRF10} and Q_{Wiasi} is of 261 (-2) mm using $k = 3$ ($k = 18$). This is increased to 334 (61 and 35) mm for R_{WRF2} using $k = 3$ and 3 ($k = 3$ and 18, and $k = 18$ and 18). This is related to the fact that WRF2 simulates significantly more precipitation as compared to WRF10 (cf. third column of Tables 1 and 6). Indeed, the difference between annual amounts of P_{WRF10} and P_{TRMM} is of 165 (-7) mm using $k = 3$ ($k = 18$). This is increased to 281 and 261 (159) mm for P_{WRF2} using $k = 3$ and 3 and $k = 3$ and 18 ($k = 18$ and 18). Accordingly, the annual runoff ratio of 6.0% obtained for WRF10 using $k = 18$ is increased to 9.2% (8.0%) for WRF2 using $k = 3$ and 18 ($k = 18$ and 18).

Similarly to what was deduced from WRF10 results in area A, the diminution of surface runoff between the WRF2 simulations with $k = 3$ and 3 and $k = 3$ and 18 is associated with a slight increase of θ_{WRF2} and ET_{WRF2} and a slight decrease of T_{WRF2} (see blue solid line with triangles in Figs. 12c–e and corresponding annual values in Table 6). This is the well-defined terrestrial segment of soil moisture–precipitation feedbacks defined by Guo et al. (2006). Also, as for area A–averaged WRF10 results, the impact of k on Sissili catchment–averaged WRF2 results, in the case of identical lateral boundary conditions, that is, $k = 3$ and 3 and $k = 3$ and 18, is rather
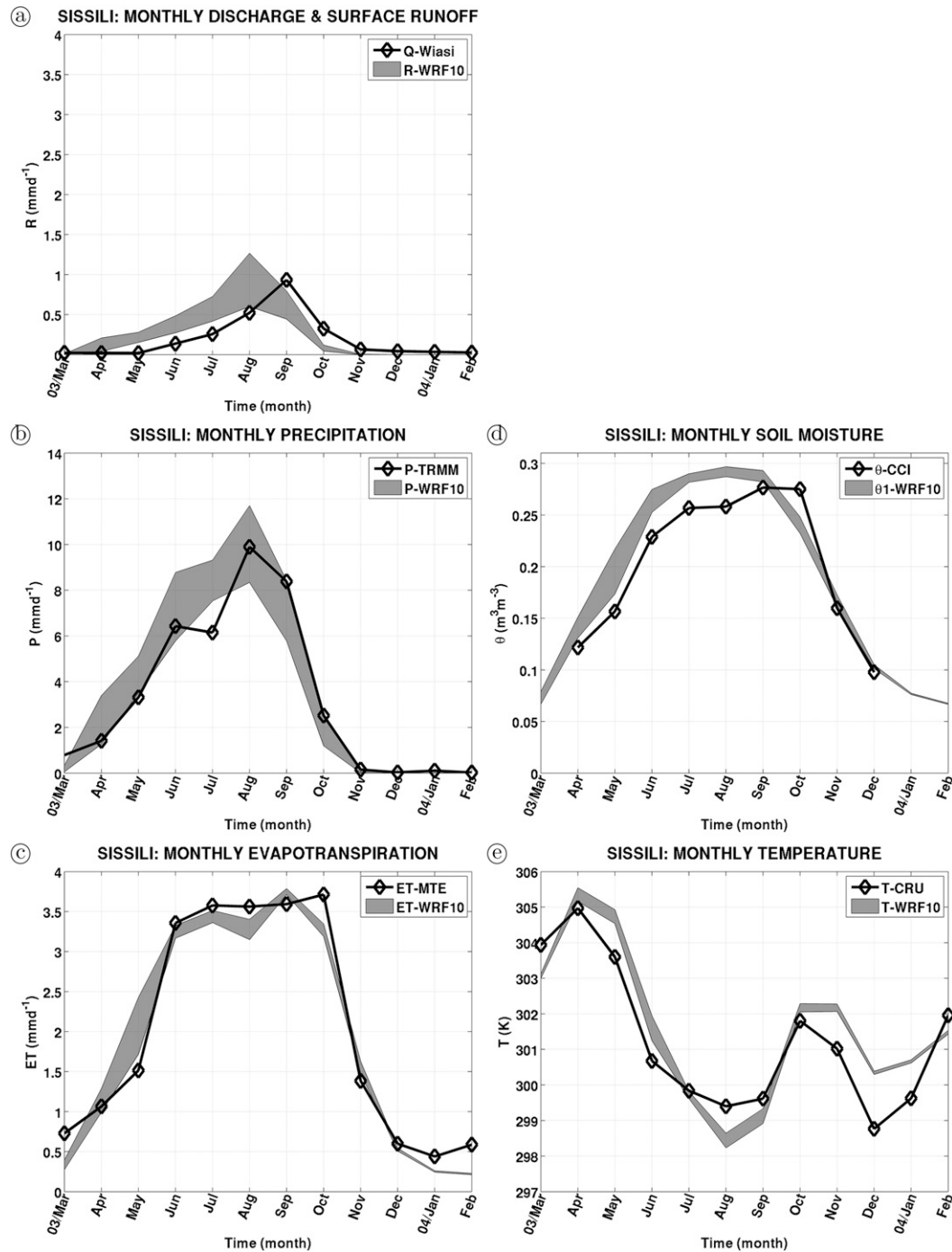
FIG. 9. As in Fig. 2, but for the seven WRF10 simulations' results with $k = 18$ using for soil moisture initial conditions the soil moisture at 0000 UTC 1 Jan 2004 from the seven WRF10 simulations with $k = 3, 6, 9, 12, 15, 18,$ and 21.

small in comparison to differences with observations. These "well-defined terrestrial segment effects" are less clear in the case with $k = 18$ and 18 because of the additional effect of a different precipitation distribution on surface fluxes in relation to different lateral boundary conditions (see green dashed line with squares in Figs. 12c–e, and corresponding annual values in Table 6).

The impact of k on WRF2 results, with identical and different lateral boundary conditions, is further quantified in Fig. 13 with mean spatial correlations of daily
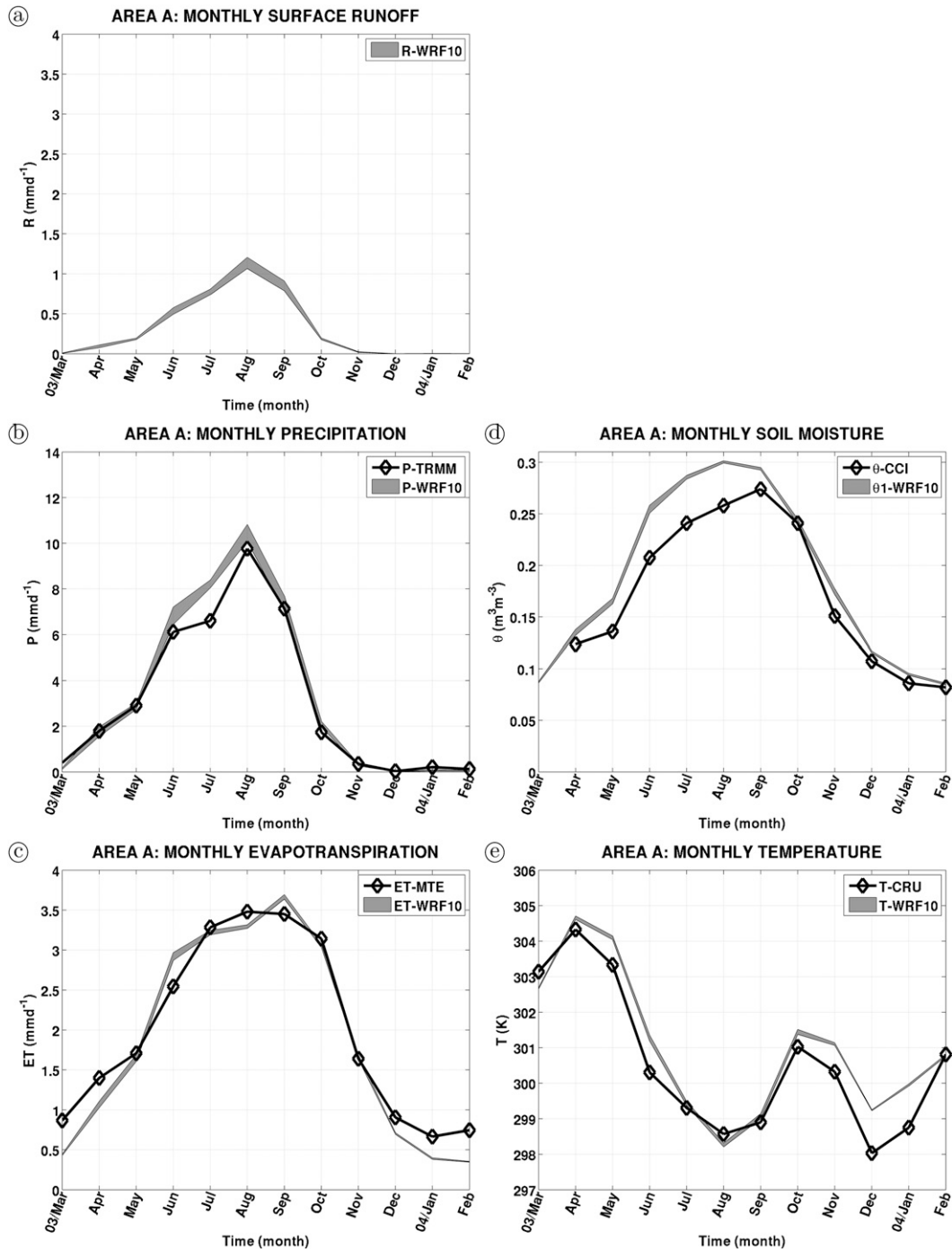
FIG. 10. As in Fig. 3, but for the seven WRF10 simulations' results with $k = 18$ using for soil moisture initial conditions the soil moisture at 0000 UTC 1 Jan 2004 from the seven WRF10 simulations with $k = 3, 6, 9, 12, 15, 18,$ and 21.

precipitation between the WRF2 simulations. These mean spatial correlations are computed for $2 \times 2 \, km^2$ subareas (grid point) in the area of the Sissili catchment and are displayed as a function of mean precipitation. In the case of unchanged lateral conditions (i.e., $k = 3$ and 3 and $k = 3$ and 18), k has some impact on the spatial

distribution of simulated daily precipitation, with mean spatial correlations between 0.4 and 0.9 (see blue triangles in Fig. 13). In the case of different lateral boundary conditions (i.e., $k = 3$ and 18 and $k = 18$ and 18) daily spatial patterns at the 2-km scale are much more different, with mean spatial correlations between -0.2
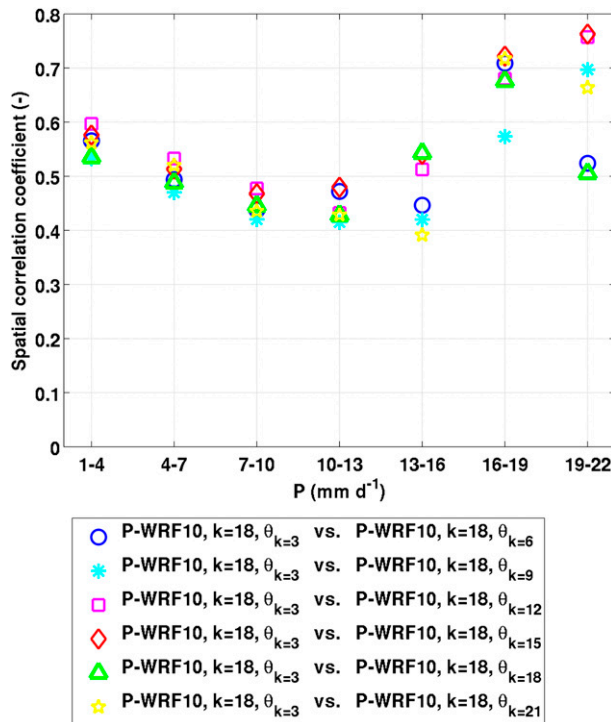
FIG. 11. As in Fig. 8, but for the seven WRF10 simulations' results with $k = 18$ using for soil moisture initial conditions the soil moisture at 0000 UTC 1 Jan 2004 from the seven WRF10 simulations with $k = 3, 6, 9, 12, 15, 18,$ and 21.

and $+0.2$ (see green squares in Fig. 13). Correlations of averaged daily and hourly precipitation time series in the Sissili catchment are accordingly very high between $k = 3$ and 3 and $k = 3$ and 18 cases, and much lower between $k = 3$ and 18 and $k = 18$ and 18 cases (see Table 7).

The above results show that there is an intrinsic spatial variability of precipitation with respect to k in the area of the Sissili catchment at 2-km resolution, which is, however, not large enough to annihilate the impact of the atmospheric forcing from the surroundings. Indeed, precipitation in West Africa is generally produced by MCSs, which on average span a distance of about 1000 km and last about 25 h (Laing et al. 2008). Therefore, precipitation patterns simulated in WRF2 (i.e., $280 \times 240 \, \text{km}^2$) are largely prescribed by the lateral

boundary conditions. The impact of k on WRF2 results in the Sissili catchment, without changing k in WRF10, would certainly have been similar to that obtained in WRF10 for a simulated area large enough to resolve MCSs' life cycles. The impact of k on WRF2 results in the case of two-way nesting would eventually be larger as well. On the other hand, a two-way nesting would create discontinuities in the soil moisture field of WRF10 because of precipitation overestimation in WRF2, resulting in artificial soil moisture–precipitation feedbacks in WRF10. Such a physical inconsistency is avoided with the one-way nesting option. In the following, the configuration of WRF2 with $k = 18$ and 18 is retained for the comparison with WRF-Hydro results since it provides the smallest precipitation and runoff annual biases, that is, 159 and 35 mm, respectively.

e. Calibration of the hydrologically enhanced inner domain (WRF-Hydro)

As in WRF, the runoff–infiltration partitioning in WRF-Hydro also has to be calibrated with k [Eq. (2)]. Here we choose to calibrate k for the WRF-Hydro inner domain (i.e., WRFH2) using $k = 18$ for the outer domain WRF10, in order to have the same lateral boundary conditions for WRFH2 and WRF2, $k = 18$ and 18. Since it was shown previously that k does not have a large impact on the annual amount of P_{WRF2} when lateral boundary conditions are fixed, in relation with the relatively small size of WRF2 domain, the annual amount of R_{WRFH2} with $k = 18$ ("calibrated value") should be comparable to that of R_{WRF2} with $k = 18$ and 18.

The sensitivity of WRFH2 results to k has been tested for several values between 3 and 1.4. The annual amount of R_{WRFH2} was much lower than that of R_{WRF2} when using the default value $k = 3$ (not shown), and among the tested values $k = 1.4$ gave an annual amount of R_{WRFH2} closest to that of R_{WRF2} (results for $k = 1.4$ are shown in Tables 6 and 7 and Figs. 12–14). The Manning's channel roughness coefficients, which do not affect R_{WRFH2}, have also been adjusted in order to improve the shape of the simulated daily discharge (Q_{WRFH2}) with respect to observation (Fig. 14b; see last column of Table 3). As compared to default values, these

TABLE 6. As in Table 1, but for the WRF2 simulations using $k = 3$ and 3, 3 and 18, and 18 and 18, and from the WRFH2 simulation using $k = 18$ and 1.4.

	Q and R (mm)	P (mm)	Runoff ratio (%)	ET (mm)	θ_1 (m^3 m^{-3})	T (K)
Obs	73	1199	6.1	737	0.204	301.26
WRF2, $k = 3$ and 3	$+334$	$+281$	27.5	-34	$+0.019$	$+0.35$
WRF2, $k = 3$ and 18	$+61$	$+261$	9.2	-8	$+0.026$	$+0.31$
WRF2, $k = 18$ and 18	$+35$	$+159$	8.0	-21	$+0.023$	$+0.25$
WRFH2, $k = 18$ and 1.4	$+19$	$+172$	6.5	-14	$+0.023$	$+0.24$

FIG. 12. As in Fig. 2, but for differences between results from the WRF2 simulations using $k = 3$ and 3, 3 and 18, and 18 and 18 and from the WRFH2 simulation using $k = 18$ and 1.4 (see legend at the bottom of the figure).
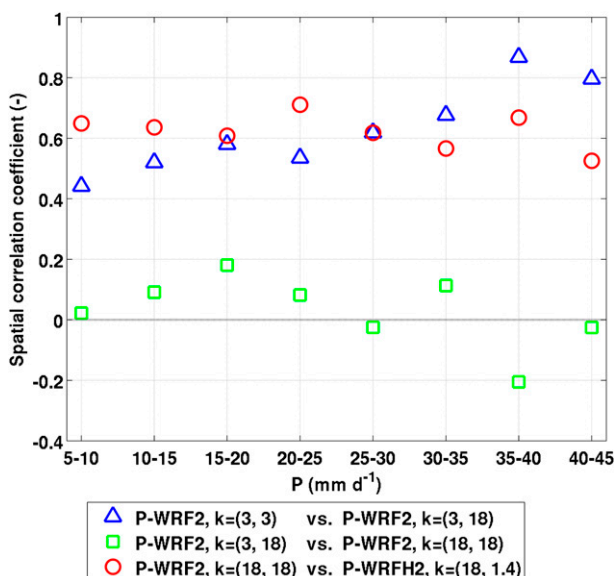
FIG. 13. As in Fig. 7, but for spatial correlations between 2 × 2 km² subareas (gridpoint resolution) of daily precipitation from the WRF2 and WRFH2 simulations in the area of the Sissili catchment (see legend at the bottom of the figure). Spatial correlations shown here are averaged for the selected bins of mean daily precipitation in the area of the Sissili catchment and plotted as a function of these bins (see x axis). Spatial correlations between P_{WRF2} with $k = 3$ and 3 and P_{WRF2} with $k = 3$ and 18 (blue triangles) are in the same range as those between P_{WRF2} with $k = 18$ and 18 and P_{WRFH2} with $k = 18$ and 1.4 (red circles) and much higher than those between P_{WRF2} with $k = 3$ and 18 and P_{WRF2} with $k = 18$ and 18 (green squares).

coefficients have been increased for the purpose of reproducing the slow discharge decrease from mid-October.

It has to be noticed that in this coupled atmospheric–hydrological model experiment these coefficients cannot be finely tuned to exactly fit modeled discharge to observations, since the bias in modeled discharge is also due to biases in modeled precipitation (see Table 6). In particular, the discharge overestimation (underestimation) in June–August (September) is associated with an overestimation (underestimation) of precipitation with

respect to TRMM, as shown in Figs. 14a and 14b. Note that in Fig. 14a daily precipitation time series have been smoothed with a 14-day Gaussian low-pass filter in order to facilitate the comparison of precipitation amounts with discharge amounts. The task of simulating accurate daily discharge with such a coupled atmospheric–hydrological approach is for this reason particularly challenging. Nevertheless, in our "calibrated" WRF-Hydro configuration a Nash–Sutcliffe model efficiency coefficient (NSE; Nash and Sutcliffe 1970) of 0.43 is achieved for the daily Wiasi discharge. A comparable WRF-Hydro performance was reported by Yucel et al. (2015) in the context of flood forecasting for selected short time episodes. Hydrological modeling studies usually involve numerical models that predict river streamflow using observed or modeled precipitation as input data (e.g., Schuol and Abbaspour 2006; Wagner et al. 2006; d'Orgeval and Polcher 2008). In these cases, observed streamflow in West African river basins are usually reproduced with an NSE between 0.2 and 0.7. Our WRF-Hydro setup not only provides a streamflow prediction with a similar accuracy, but it also gives the possibility to investigate hydrological feedbacks on precipitation.

It is finally noted that two very different calibrated values of k between two WRF and WRF-Hydro simulation give comparable monthly and daily surface runoff (see Figs. 12a, 15). This is certainly related to the different description of runoff–infiltration partitioning between WRF and WRF-Hydro. Indeed, in WRF-Hydro the infiltration excess of Eq. (2) is ponded so that it can partially infiltrate at the next time step if not discharged in a stream grid cell. On the other hand, in WRF the surface water is not ponded but goes directly to surface runoff. Our result suggests that increasing WRF-resolved surface infiltration (increase of k) leads to a simulated annual, monthly, and daily surface runoff relatively close to that from WRF-Hydro. In the following section we compare the effect of these two different physical descriptions of runoff–infiltration partitioning on modeled land–atmosphere feedbacks,

TABLE 7. Correlation coefficients between each pair of TRMM-, WRF2-, and WRFH2-derived precipitation time series for the Sissili catchment for the period April–November 2003, at daily (italics) and hourly (boldface) resolution. Note that TRMM is a 3-hourly product, so there is no hourly correlation.

	P_{WRF2}, $k = 3$ and 3	P_{WRF2}, $k = 3$ and 18	P_{WRF2}, $k = 18$ and 18	P_{WRFH2}, $k = 18$ and 1.4
P_{TRMM}	*0.19*	*0.19*	*0.23*	*0.23*
P_{WRF2}, $k = 3$ and 3		*0.99*	*0.51*	*0.51*
		0.99	**0.19**	**0.19**
P_{WRF2}, $k = 3$ and 18			*0.51*	*0.51*
			0.20	**0.19**
P_{WRF2}, $k = 18$ and 18				*0.99*
				0.99

FIG. 14. (a) Daily time series of 14-day Gaussian low-pass-filtered daily precipitation averaged in the area of the Sissili catchment, from TRMM (gray dash–dotted line) and from the WRFH2 simulation using $k = 18$ and 1.4 and the calibrated Manning coefficients of Table 3 (blue dashed line). (b) As in (a), but for daily discharge at Wiasi from the gauge observation and the WRH2 simulation. The NSE is indicated.

that is, changes in atmospheric variables like precipitation when overland flow is enabled.

f. Sensitivity of inner domain results to enabled overland flow

WRF2 results using $k = 18$ and 18 are compared here with WRFH2 results using $k = 18$ and 1.4. The same daily peaks are present in R_{WRFH2} and R_{WRF2} (no side values in the scatterplot of Fig. 15), indicating that similar precipitation events at the scale of the Sissili catchment are simulated in WRFH2 and WRF2. This is confirmed by high correlation coefficients of daily and hourly precipitation time series (Table 7) and relatively high spatial correlations of $2 \times 2 \, km^2$ subareas of daily precipitation (see red circles in Fig. 13).

The fact that R_{WRFH2} is generally lower than R_{WRF2} at the beginning of the wet season (until July; see Fig. 12a) is coherent with drier soils/higher infiltration capacity at this time of the year (e.g., Fig. 5a). Indeed, surface routing in WRF-Hydro allows precipitation to infiltrate in a larger area than in WRF, which results in more infiltration when soils are dry. Accordingly, θ_{WRFH2} and ET_{WRFH2} are slightly higher than θ_{WRF2} and ET_{WRF2} until August (cf. green dashed lines with squares and red dashed lines with circles in Figs. 12c,d). However, this effect is very small and the impact on temperature is hardly visible in Fig. 12e. Values of P_{WRFH2} and P_{WRF2} are also generally close, except in July, when WRFH2 slightly increases the monthly difference with TRMM (Fig. 12b) and the annual amount as well (Table 6). Altogether, the different treatment of runoff–infiltration partitioning between WRF2 with $k = 18$ and 18 and WRFH2 with $k = 18$ and 1.4 leads to precipitation

results' differences, that is, increase of annual precipitation by 13 mm and spatial correlations between 0.52 and 0.71, comparable to the differences obtained between WRF2 with $k = 3$ and 3 and WRF2 with $k = 3$ and 18, that is, decrease of annual precipitation by 20 mm and spatial correlations between 0.44 and 0.87 (see Tables 6 and 7, Figs. 12 and 13). It is therefore concluded here that the additional description of overland flow in WRF-Hydro has a clear impact on simulated precipitation, via overland flow–induced changes
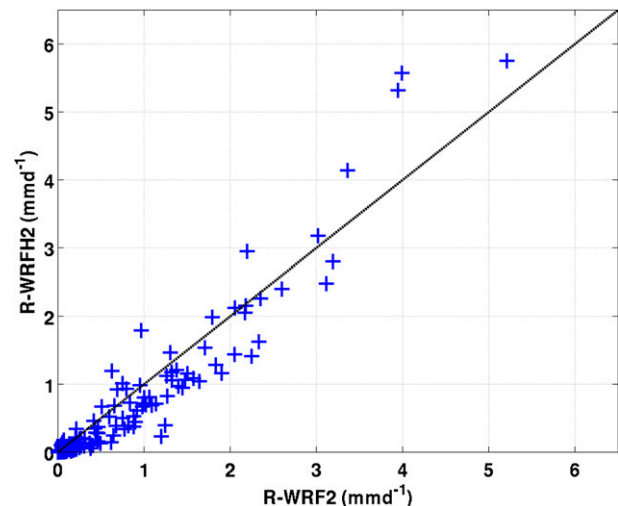
FIG. 15. Scatterplot between Sissili catchment–averaged daily surface runoff (mm day^{-1}) from the WRF2 simulation with $k = 18$ and 18 (R_{WRF2}; x axis) and that from the WRFH2 simulation using $k = 18$ and 1.4 and the calibrated Manning coefficients of Table 3 (R_{WRFH2}; y axis).

in runoff–infiltration partitioning and land–atmosphere feedback mechanisms, especially at the beginning of the wet season when soils are still dry (soil moisture–limited ET regime). As for WRF2, this impact would probably be significant at the scale of the Sissili catchment in the case of a simulated area large enough to resolve the interaction between land surface and MCSs through their entire life cycle.

6. Summary and perspectives

The first application of a fully coupled atmospheric–hydrological modeling system, that is, WRF-Hydro, for West Africa was presented. The fully coupled modeling system allowed for modeling of the complete regional water cycle, from the top of the atmosphere, via the boundary layer, to the land surface, the unsaturated zone, and the flow in the river beds. Only atmospheric inflow and outflow at the coarsest model domain were prescribed; no additional hydrometeorological driving information is needed in this approach. Our focus here was on the role of runoff–infiltration partitioning and resolved overland flow on land–atmosphere feedbacks, particularly precipitation.

A two-domain WRF setup using a one-way nesting technique was applied, with an outer domain at 10-km resolution encompassing the West African continent and an inner domain centered on the Sissili catchment. In our WRF-Hydro setup, the computation of runoff–infiltration partitioning in the inner domain was enhanced with overland flow and streamflow routing on a subgrid at 500-m resolution (Fig. 1).

The role of runoff–infiltration partitioning on land–atmosphere feedbacks was deduced from a sensitivity of WRF outer domain results to the runoff–infiltration partitioning parameter k. The range of annual precipitation variation to this parameter was about one-sixth of the annual amount. Setting it to 18 resulted in simulated annual runoff and annual precipitation in the Sissili catchment closest to observations. However, this result was mitigated by the fact that a comparable annual precipitation spread was obtained for a fixed value of the runoff–infiltration partitioning parameter but varied soil moisture initial condition. Runoff–infiltration partitioning calibration also had an effect on other observed atmospheric–hydrological characteristics of the Sissili catchment, that is, 3-hourly, daily, and monthly precipitation; monthly evapotranspiration; monthly soil moisture; and monthly temperature. This impact was much reduced for the entire West African Sudano-Sahelian region (area A, see Fig. 1a).

A similar sensitivity analysis was conducted for the WRF inner domain, modifying the runoff–infiltration partitioning parameter separately in the outer and inner domain. Keeping this parameter constant in the outer domain, the impact of varying it only in the inner domain was not as significant as for the outer domain for the area of the Sissili catchment, in relation with the fact that precipitation patterns simulated in the one-way nested inner domain were mainly prescribed by identical lateral boundary conditions from the outer domain. It was concluded that the impact of runoff–infiltration partitioning calibration on inner domain's precipitation results would have been similar to that obtained in the outer domain for a larger simulated area.

Setting the runoff–infiltration partitioning parameter to 18 for both outer and inner domains resulted in outer and inner domains' annual runoff and annual precipitation in the Sissili catchment closest to observations, although annual precipitation in the inner domain was generally 10%–15% higher than that in the outer domain. Setting this parameter to 1.4 for the WRF-Hydro inner domain gave comparable annual amounts of surface runoff and precipitation. Indeed, in WRF-Hydro the infiltration excess is ponded and routed on the subgrid at 500-m resolution so that it can partially infiltrate at the next time step if not discharged in a stream grid cell of the subgrid. Since surface water is not ponded in WRF, WRF-resolved surface infiltration has to be increased (increase of k) in order to obtain a runoff–infiltration partitioning closer to that in WRF-Hydro.

Analysis of hydrological feedbacks revealed that WRF-Hydro predicted more infiltration and less runoff at the beginning of the wet season, when soils were still dry, although the impact on evapotranspiration, temperature, and precipitation was small. The impact of overland routing on precipitation, via overland flow–induced changes in runoff–infiltration partitioning and land–atmosphere feedback mechanisms, is assumed to be much larger for simulated areas large enough to resolve MCSs' life cycles. The WRF-Hydro simulation finally allowed for reproduction of daily streamflow in the river bed with a reasonable performance (NSE of 0.43).

Hydrological Service Department of the Ministry of Water Resources, Works and Housing of Ghana. Technical information about HydroSHEDS data is available online at http://hydrosheds.cr.usgs.gov. The WRF-Hydro preprocessing tool is available online at https://www.ral.ucar.edu/sites/default/files/public/projects/wrf_hydro/v3_0/Standalone_Tool_v2_2.zip. WRF and WRF-Hydro simulations were run at the German Climate Computing Center. Test simulations were run at the Leibniz-Rechenzentrum. We are thankful to Christof Lorenz for helping acquiring the observational data products; to Dave Gochis, Kevin Sampson, and Christoph Sörgel for the WRF-Hydro and ArcGIS support; to Irina Fast for computer support at the German Climate Computing Center; to Ibrahim Boubacar, Jakob Garvelmann, Gero Steup, Aaron Boone, and Alfonso Senatore for fruitful discussions on West African hydrology; to Bamba Sylla, Dominikus Heinzeller, and Cornelia Klein for sharing ideas about regional atmospheric modeling in West Africa; and to two reviewers for their constructive remarks.

REFERENCES

Adler, B., N. Kalthoff, and L. Gantner, 2011: Initiation of deep convection caused by land-surface inhomogeneities in West Africa: A modelled case study. *Meteor. Atmos. Phys.*, **112**, 15–27, doi:10.1007/s00703-011-0131-2.

Agustí-Panareda, A., G. Balsamo, and A. Beljaars, 2010: Impact of improved soil moisture on the ECMWF precipitation forecast in West Africa. *Geophys. Res. Lett.*, **37**, L20808, doi:10.1029/2010GL044748.

Albergel, C., and Coauthors, 2008: From near-surface to root-zone soil moisture using an exponential filter: An assessment of the method based on in-situ observations and model simulations. *Hydrol. Earth Syst. Sci.*, **12**, 1323–1337, doi:10.5194/hess-12-1323-2008.

Anyah, R. O., C. P. Weaver, G. Miguez-Macho, Y. Fan, and A. Robock, 2008: Incorporating water table dynamics in climate modeling: 3. Simulated groundwater influence on coupled land–atmosphere variability. *J. Geophys. Res.*, **113**, D0703, doi:10.1029/2007JD009087.

Bliefernicht, J., and Coauthors, 2013: Field and simulation experiments for investigating regional land–atmosphere interactions in West Africa: Experimental setup and first results. *IAHS Publ.*, **359**, 226–232.

Bonsor, H. C., and A. M. MacDonald, 2011: An initial estimate of depth to groundwater across Africa. British Geological Survey Open Rep. OR/11/067, 26 pp.

Brocca, L., and Coauthors, 2011: Soil moisture estimation through ASCAT and AMSR-E sensors: An intercomparison and validation study across Europe. *Remote Sens. Environ.*, **115**, 3390–3408, doi:10.1016/j.rse.2011.08.003.

Browne, N. A. K., and M. B. Sylla, 2012: Regional climate model sensitivity to domain size for the simulation of the West African summer monsoon rainfall. *Int. J. Geophys.*, **2012**, 625831, doi:10.1155/2012/625831.

Casenave, A., and C. Valentin, 1992: A runoff capability classification system based on surface features criteria in semi-arid areas of West Africa. *J. Hydrol.*, **130**, 231–249, doi:10.1016/0022-1694(92)90112-9.

Chen, F., and J. Dudhia, 2001: Coupling an advanced land surface–hydrology model with the Penn State–NCAR MM5 Modeling System. Part I: Model implementation and sensitivity. *Mon. Wea. Rev.*, **129**, 569–585, doi:10.1175/1520-0493(2001)129<0569:CAALSH>2.0.CO;2.

——, and Y. Zhang, 2009: On the coupling strength between the land surface and the atmosphere: From viewpoint of surface exchange coefficients. *Geophys. Res. Lett.*, **36**, L10404, doi:10.1029/2009GL037980.

Chevallier, P., and O. Planchon, 1993: Hydrological processes in a small humid savanna basin (Ivory Coast). *J. Hydrol.*, **151**, 173–191, doi:10.1016/0022-1694(93)90235-2.

Csiszar, I., and G. Gutman, 1999: Mapping global land surface albedo from NOAA/AVHRR. *J. Geophys. Res.*, **104**, 6215–6228, doi:10.1029/1998JD200090.

Dee, D. P., and Coauthors, 2011: The ERA-Interim reanalysis: Configuration and performance of the data assimilation system. *Quart. J. Roy. Meteor. Soc.*, **137**, 553–597, doi:10.1002/qj.828.

Delire, C., N. de Noblet-Ducoudré, A. Sima, and I. Gouirand, 2011: Effect of vegetation dynamics on climate variability: Contrasting results from two modeling studies. *J. Climate*, **24**, 2238–2257, doi:10.1175/2010JCLI3664.1.

Descroix, L., and Coauthors, 2009: Spatio-temporal variability of hydrological regimes around the boundaries between Sahelian and Sudanian areas of West Africa: A synthesis. *J. Hydrol.*, **375**, 90–102, doi:10.1016/j.jhydrol.2008.12.012.

Dirmeyer, P. A., 2011: The terrestrial segment of soil moisture–climate coupling. *Geophys. Res. Lett.*, **38**, L16702, doi:10.1029/2011GL048268.

d'Orgeval, T., and J. Polcher, 2008: Impacts of precipitation events and land-use changes on West African river discharges during the years 1951–2000. *Climate Dyn.*, **31**, 249–262, doi:10.1007/s00382-007-0350-x.

Dorigo, W. A., and Coauthors, 2014: Evaluation of the ESA CCI soil moisture product using ground-based observations. *Remote Sens. Environ.*, **162**, 380–395, doi:10.1016/j.rse.2014.07.023.

Dudhia, J., 1989: Numerical study of convection observed during the Winter Monsoon Experiment using a mesoscale two-dimensional model. *J. Atmos. Sci.*, **46**, 3077–3107, doi:10.1175/1520-0469(1989)046<3077:NSOCOD>2.0.CO;2.

Dunne, T., 1978: Field studies of hillslope flow processes. *Hillslope Hydrology*, J. J. Kirkby, Ed., Wiley, 227–293.

Ek, M. B., K. E. Mitchell, Y. Lin, E. Rogers, P. Grummann, V. Koren, G. Gayno, and J. D. Tarpley, 2003: Implementation of Noah land surface model advances in the National Centers for Environmental Prediction operational Mesoscale Eta Model. *J. Geophys. Res.*, **108**, 8851, doi:10.1029/2002JD003296.

Esteves, M., and J. M. Lapetite, 2003: A multi-scale approach of runoff generation in a Sahelian gully catchment: A case study in Niger. *Catena*, **50**, 255–271, doi:10.1016/S0341-8162(02)00136-4.

Findell, K. L., and E. A. Eltahir, 2003: Atmospheric controls on soil moisture–boundary layer interactions: Three-dimensional wind effects. *J. Geophys. Res.*, **108**, 8385, doi:10.1029/2001JD001515.

Friedl, M. A., and Coauthors, 2002: Global land cover mapping from MODIS: Algorithms and early results. *Remote Sens. Environ.*, **83**, 287–302, doi:10.1016/S0034-4257(02)00078-0.

Froidevaux, P., L. Schlemmer, J. Schmidli, W. Langhans, and C. Schär, 2014: Influence of the background wind on the local soil moisture–precipitation feedbacks. *J. Atmos. Sci.*, **71**, 782–799, doi:10.1175/JAS-D-13-0180.1.

Gantner, L., and N. Kalthoff, 2010: Sensitivity of a modelled life cycle of a mesoscale convective system to soil conditions over West Africa. *Quart. J. Roy. Meteor. Soc.*, **136**, 471–482, doi:10.1002/qj.425.

Gochis, D., and F. Chen, 2003: Hydrological enhancements to the community Noah land surface model. NCAR Scientific Tech. Rep., 77 pp. [Available online at http://nldr.library.ucar.edu/repository/assets/technotes/TECH-NOTE-000-000-000-516.pdf.]

——, W. Yu, and D. N. Yates, 2014: The WRF-Hydro model technical description and user's guide, version 2.0. NCAR Tech. Doc., 120 pp. [Available online at https://www.ral.ucar.edu/projects/wrf_hydro.]

Grell, G., J. Dudhia, and D. Stauffer, 1994: A description of the Fifth generation Penn State/NCAR Mesoscale Model (MM5). NCAR Tech. Note NCAR/TN-398+STR, 121 pp., doi:10.5065/D60Z716B.

Guo, Z., and Coauthors, 2006: GLACE: The Global Land–Atmosphere Coupling Experiment. Part II: Analysis. J. Hydrometeor., 7, 611–625, doi:10.1175/JHM511.1.

Gutman, G., and A. Ignatov, 1998: The derivation of the green vegetation fraction from NOAA/AVHRR data for use in numerical weather prediction models. Int. J. Remote Sens., 19, 1533–1543, doi:10.1080/014311698215333.

Hagos, S. M., L. Y. R. Leung, Y. Xue, A. Boone, F. de Sales, N. Neupane, M. Huang, and J. H. Yoon, 2014: Assessment of uncertainties in the response of the African monsoon precipitation to land use change simulated by a regional model. Climate Dyn., 43, 2765–2775, doi:10.1007/s00382-014-2092-x.

Harris, I., P. D. Jones, T. J. Osborn, and D. H. Lister, 2014: Updated high-resolution grids of monthly climatic observations—The CRU TS3.10 dataset. Int. J. Climatol., 34, 623–642, doi:10.1002/joc.3711.

Hong, S.-Y., J. Dudhia, and S.-H. Chen, 2004: A revised approach to ice microphysical processes for the bulk parameterization of clouds and precipitation. Mon. Wea. Rev., 132, 103–120, doi:10.1175/1520-0493(2004)132<0103:ARATIM>2.0.CO;2.

——, Y. Noh, and J. Dudhia, 2006: A new vertical diffusion package with an explicit treatment of entrainment processes. Mon. Wea. Rev., 134, 2318–2341, doi:10.1175/MWR3199.1.

Huffman, G. J., and Coauthors, 2007: The TRMM Multi-Satellite Precipitation Analysis: Quasi-global, multi-year, combined-sensor precipitation estimates at fine scale. J. Hydrometeor., 8, 38–55, doi:10.1175/JHM560.1.

Jones, J. E., and C. S. Woodward, 2001: Preconditioning Newton–Krylov methods for variably saturated flow. Adv. Water Resour., 24, 763–774, doi:10.1016/S0309-1708(00)00075-0.

Julien, P. Y., B. Saghafian, and F. L. Ogden, 1995: Raster-based hydrologic modeling of spatially-varied surface runoff. J. Amer. Water Resour. Assoc., 31, 523–536, doi:10.1111/j.1752-1688.1995.tb04039.x.

Jung, G., S. Wagner, and H. Kunstmann, 2012: Joint climate–hydrology modeling: An impact study for the data-sparse environment of the Volta basin in West Africa. Hydrol. Res., 43, 231–248, doi:10.2166/nh.2012.044.

Jung, M., M. Reichstein, and A. Bondeau, 2009: Towards global empirical upscaling of FLUXNET eddy covariance observations: Validation of a model tree ensemble approach using a biosphere model. Biogeosciences, 6, 2001–2013, doi:10.5194/bg-6-2001-2009.

——, and Coauthors, 2010: Recent decline in the global land evapotranspiration trend due to limited moisture supply. Nature, 467, 951–954, doi:10.1038/nature09396.

Kain, J. S., 2004: The Kain–Fritsch convective parameterization: An update. J. Appl. Meteor., 43, 170–181, doi:10.1175/1520-0450(2004)043<0170:TKCPAU>2.0.CO;2.

Klein, C., D. Heinzeller, J. Bliefernicht, and H. Kunstmann, 2015: Variability of West African monsoon patterns generated by a WRF multi-physics ensemble. Climate Dyn., 45, 2733–2755, doi:10.1007/s00382-015-2505-5.

Koster, R. D., and Coauthors, 2004: Regions of strong coupling between soil moisture and precipitation. Science, 305, 1138–1140, doi:10.1126/science.1100217.

——, and Coauthors, 2006: GLACE: The Global Land–Atmosphere Coupling Experiment. Part I: Overview. J. Hydrometeor., 7, 590–610, doi:10.1175/JHM510.1.

——, S. Mahanama, and T. Yamada, 2010: Contribution of land surface initialization to subseasonal forecast skill: First results from a multi-model experiment. Geophys. Res. Lett., 37, L02402, doi:10.1029/2009GL041677.

——, Y. Chang, and S. Schubert, 2014: A mechanism for land–atmosphere feedback involving planetary wave structures. J. Climate, 27, 9290–9301, doi:10.1175/JCLI-D-14-00315.1.

Kumar, A., F. Chen, M. Barlage, M. B. Ek, and D. Niyogi, 2014: Assessing impacts of integrating MODIS vegetation data in the Weather Research and Forecasting (WRF) Model coupled to two different canopy-resistance approaches. J. Appl. Meteor. Climatol., 53, 1362–1380, doi:10.1175/JAMC-D-13-0247.1.

Kunstmann, H., and G. Jung, 2007: Influence of soil-moisture and land use change on precipitation in the Volta basin of West Africa. Int. J. River Basin Manage., 5, 9–16, doi:10.1080/15715124.2007.9635301.

Laing, A. G., R. E. Carbone, V. Levizzani, and J. D. Tuttle, 2008: The propagation and diurnal cycles of deep convection in northern tropical Africa. Quart. J. Roy. Meteor. Soc., 134, 93–109, doi:10.1002/qj.194.

Larsen, M. A. D., J. C. Refsgaard, M. Drews, M. B. Butts, K. H. Jensen, J. Christensen, and O. Christensen, 2014: Results from a full coupling of the HIRHAM regional climate model and the MIKE SHE hydrological model for a Danish catchment. Hydrol. Earth Syst. Sci., 18, 4733–4749, doi:10.5194/hess-18-4733-2014.

Lebel, T., and Coauthors, 2009: AMMA-CATCH studies in the Sahelian region of West-Africa: An overview. J. Hydrol., 375, 3–13, doi:10.1016/j.jhydrol.2009.03.020.

Lehner, B., K. Verdin, and A. Jarvis, 2008: New global hydrography derived from spaceborne elevation data. Eos, Trans. Amer. Geophys. Union, 89, 93–94, doi:10.1029/2008EO100001.

Lohou, F., and Coauthors, 2014: Surface response to rain events throughout the West African monsoon. Atmos. Chem. Phys., 14, 3883–3898, doi:10.5194/acp-14-3883-2014.

Lorenz, C., H. Kunstmann, B. Devaraju, M. J. Tourian, N. Sneeuw, and J. Riegger, 2014: Large-scale runoff from landmasses: A global assessment of the closure of the hydrological and atmospheric water balances. J. Hydrometeor., 15, 2111–2139, doi:10.1175/JHM-D-13-0157.1.

Ma, L.-M., and Z.-M. Tan, 2009: Improving the behavior of the cumulus parameterization for tropical cyclone prediction: Convection trigger. Atmos. Res., 92, 190–211, doi:10.1016/j.atmosres.2008.09.022.

Marsham, J. H., N. Dixon, L. Garcia-Carreras, G. M. S. Lister, D. J. Parker, P. Knippertz, and C. Birch, 2013: The role of moist convection in the West African monsoon system: Insights from continental-scale convection-permitting simulations. Geophys. Res. Lett., 40, 1843–1849, doi:10.1002/grl.50347.

Maxwell, R. M., F. K. Chow, and S. J. Kollet, 2007: The groundwater–land-surface–atmosphere connection: Soil moisture effects on the atmospheric boundary layer in fully-coupled simulations. Adv. Water Resour., 30, 2447–2466, doi:10.1016/j.advwatres.2007.05.018.

——, J. K. Lundquist, J. D. Mirocha, S. G. Smith, C. S. Woodward, and A. F. Tompson, 2011: Development of a coupled

groundwater–atmosphere model. *Mon. Wea. Rev.*, **139**, 96–116, doi:10.1175/2010MWR3392.1.

Miguez-Macho, G., Y. Fan, C. P. Weaver, R. Walko, and A. Robock, 2007: Incorporating water table dynamics in climate modeling: 2. Formulation, validation, and soil moisture simulation. *J. Geophys. Res.*, **112**, D13108, doi:10.1029/2006JD008112.

Miralles, D. G., R. A. M. de Jeu, J. H. Gash, T. R. H. Holmes, and A. J. Dolman, 2011: Magnitude and variability of land evaporation and its components at the global scale. *Hydrol. Earth Syst. Sci.*, **15**, 967–981, doi:10.5194/hess-15-967-2011.

Mlawer, E. J., S. J. Taubman, P. D. Brown, M. J. Iacono, and S. A. Clough, 1997: Radiative transfer for inhomogeneous atmospheres: RRTM, a validated correlated-*k* model for the longwave. *J. Geophys. Res.*, **102**, 16 663–16 682, doi:10.1029/97JD00237.

Moufouma-Okia, W., and D. P. Rowell, 2009: Impact of soil moisture initialisation and lateral boundary conditions on regional climate model simulations of the West African Monsoon. *Climate Dyn.*, **35**, 213–229, doi:10.1007/s00382-009-0638-0.

Mu, Q., F. A. Heinsch, M. Zhao, and S. W. Running, 2007: Development of a global evapotranspiration algorithm based on MODIS and global meteorology data. *Remote Sens. Environ.*, **111**, 519–536, doi:10.1016/j.rse.2007.04.015.

——, M. Zhao, and S. W. Running, 2011: Improvements to a MODIS global terrestrial evapotranspiration algorithm. *Remote Sens. Environ.*, **115**, 1781–1800, doi:10.1016/j.rse.2011.02.019.

Nash, J. E., and J. V. Sutcliffe, 1970: River flow forecasting through conceptual models part I—A discussion of principles. *J. Hydrol.*, **10**, 282–290, doi:10.1016/0022-1694(70)90255-6.

Nicholson, S. E., 2000: Land surface processes and Sahel climate. *Rev. Geophys.*, **38**, 117–139, doi:10.1029/1999RG900014.

——, 2013: The West African Sahel: A review of recent studies on the rainfall regime and its interannual variability. *ISRN Meteor.*, **2013**, 453521, doi:10.1155/2013/453521.

——, and Coauthors, 2003: Validation of TRMM and other rainfall estimates with a high-density gauge dataset for West Africa. Part II: Validation of TRMM rainfall products. *J. Appl. Meteor.*, **42**, 1355–1368, doi:10.1175/1520-0450(2003)042<1355:VOTAOR>2.0.CO;2.

Ogden, F. L., 1997: CASC2D reference manual. Dept. of Civil and Environmental Engineering, University of Connecticut, 83 pp.

Pal, J. S., and Coauthors, 2007: The ICTP RegCM3 and RegCNET: Regional climate modeling for the developing world. *Bull. Amer. Meteor. Soc.*, **88**, 1395–1409, doi:10.1175/BAMS-88-9-1395.

Peugeot, C., M. Esteves, S. Galle, J. L. Rajot, and J. P. Vandervaere, 1997: Runoff generation processes: Results and analysis of field data collected at the central supersite of the HAPEX-Sahel experiment. *J. Hydrol.*, **188–189**, 179–202, doi:10.1016/S0022-1694(96)03159-9.

——, and Coauthors, 2011: Meso-scale water cycle within the West African monsoon. *Atmos. Sci. Lett.*, **12**, 45–50, doi:10.1002/asl.309.

Pielke, R. A., Sr., 2001: Influence of the spatial distribution of vegetation and soils on the prediction of cumulus convective rainfall. *Rev. Geophys.*, **39**, 151–177, doi:10.1029/1999RG000072.

Redelsperger, J.-L., C. D. Thorncroft, A. Diedhiou, T. Lebel, D. J. Parker, and J. Polcher, 2006: African monsoon multidisciplinary analysis. *Bull. Amer. Meteor. Soc.*, **87**, 1739–1746, doi:10.1175/BAMS-87-12-1739.

Santanello, J. A., S. V. Kumar, C. D. Peters-Lidard, K. Harisson, and S. Zhou, 2013: Impact of land model calibration on coupled land–atmosphere prediction. *J. Hydrometeor.*, **14**, 1373–1400, doi:10.1175/JHM-D-12-0127.1.

Schaake, J. C., V. I. Koren, Q.-Y. Duan, K. Mitchell, and F. Chen, 1996: Simple water balance model for estimating runoff at

different spatial and temporal scales. *J. Geophys. Res.*, **101**, 7461–7475, doi:10.1029/95JD02892.

Schättler, U., G. Doms, and C. Schraff, 2008: A description of the nonhydrostatic regional COSMO model. Part VII: User's guide. Deutscher Wetterdienst, 194 pp. [Available online at http://www.cosmo-model.org/content/model/documentation/core/cosmoUserGuide.pdf.]

Schenk, H. J., and R. B. Jackson, 2005: Mapping the global distribution of deep roots in relation to climate and soil characteristics. *Geoderma*, **126**, 129–140, doi:10.1016/j.geoderma.2004.11.018.

Schulla, J., and K. Jasper, 2007: Model Description WaSiM-ETH. ETH Zürich, 181 pp. [Available online at http://www.wasim.ch/downloads/doku/wasim/wasim_2007_en.pdf.]

Schuol, J., and K. C. Abbaspour, 2006: Calibration and uncertainty issues of a hydrologic model (SWAT) applied to West Africa. *Adv. Geosci.*, **9**, 137–143, doi:10.5194/adgeo-9-137-2006.

Schwendike, J., N. Kalthoff, and M. Kohler, 2010: The impact of mesoscale convective systems on the surface and boundary layer structure in West Africa: Case-studies from the AMMA campaign 2006. *Quart. J. Roy. Meteor. Soc.*, **136**, 566–582, doi:10.1002/qj.599.

Seneviratne, S. I., D. Lüthi, M. Litschi, and C. Schär, 2006: Land–atmosphere coupling and climate change in Europe. *Nature*, **443**, 205–209, doi:10.1038/nature05095.

——, T. Corti, E. L. Davin, M. Hirschi, E. B. Jaeger, I. Lehner, B. Orlowsky, and A. J. Teuling, 2010: Investigating soil moisture–climate interactions in a changing climate: A review. *Earth-Sci. Rev.*, **99**, 125–161, doi:10.1016/j.earscirev.2010.02.004.

Shrestha, P., M. Sulis, M. Masbou, S. Kollet, and C. Simmer, 2014: A scale-consistent terrestrial systems modeling platform based on COSMO, CLM, and ParFlow. *Mon. Wea. Rev.*, **142**, 3466–3483, doi:10.1175/MWR-D-14-00029.1.

Skamarock, W. C., and J. B. Klemp, 2008: A time-split nonhydrostatic atmospheric model for weather research and forecasting applications. *J. Comput. Phys.*, **227**, 3465–3485, doi:10.1016/j.jcp.2007.01.037.

Smiatek, G., H. Kunstmann, and J. Werhahn, 2012: Implementation and performance analysis of a high resolution coupled numerical weather and river runoff prediction model system for an Alpine catchment. *Environ. Modell. Software*, **38**, 231–243, doi:10.1016/j.envsoft.2012.06.001.

Stéfanon, M., P. Drobinski, F. D'Andrea, and N. de Noblet-Ducoudré, 2012: Effects of interactive vegetation phenology on the 2003 summer heat waves. *J. Geophys. Res.*, **117**, D24103, doi:10.1029/2012JD018187.

Steiner, A., J. Pal, S. Rauscher, J. Bell, N. Diffenbaugh, A. Boone, L. Sloan, and F. Giorgi, 2009: Land surface coupling in regional climate simulations of the West African monsoon. *Climate Dyn.*, **33**, 869–892, doi:10.1007/s00382-009-0543-6.

Strahler, A. N., 1957: Quantitative analysis of watershed geomorphology. *Trans. Am. Geophys. Union*, **38**, 913–920, doi:10.1029/TR038i006p00913.

Taylor, C. M., D. J. Parker, and P. P. Harris, 2007: An observational case study of mesoscale atmospheric circulations induced by soil moisture. *Geophys. Res. Lett.*, **34**, L15801, doi:10.1029/2007GL030572.

——, A. Gounou, F. Guichard, P. P. Harris, R. J. Ellis, F. Couvreux, and M. De Kauwe, 2011a: Frequency of Sahelian storm initiation enhanced over mesoscale soil-moisture patterns. *Nat. Geosci.*, **4**, 430–433, doi:10.1038/ngeo1173.

——, and Coauthors, 2011b: New perspectives on land–atmosphere feedbacks from the African Monsoon Multidisciplinary Analysis. *Atmos. Sci. Lett.*, **12**, 38–44, doi:10.1002/asl.336.

Thiemig, V., R. Rojas, M. Zambrano-Bigiarini, V. Levizzani, and A. De Roo, 2012: Validation of satellite-based precipitation

products over sparsely gauged African river basins. *J. Hydrometeor.*, **13**, 1760–1783, doi:10.1175/JHM-D-12-032.1.

van den Hurk, B. J. J. M., and E. van Meijgaard, 2010: Diagnosing land–atmosphere interaction from a regional climate model simulation over West Africa. *J. Hydrometeor.*, **11**, 467–481, doi:10.1175/2009JHM1173.1.

Vieux, B. E., 2001: *Distributed Hydrologic Modeling Using GIS*. Kluwer Academic, 289 pp.

Wagner, S., H. Kunstmann, and A. Bárdossy, 2006: Model based distributed water balance monitoring of the White Volta catchment in West Africa through coupled meteorological–hydrological simulations. *Adv. Geosci.*, **9**, 39–44, doi:10.5194/adgeo-9-39-2006.

Walko, R. L., and Coauthors, 2000: Coupled atmosphere–biophysics–hydrology models for environmental modeling. *J. Appl. Meteor.*, **39**, 931–944, doi:10.1175/1520-0450(2000)039<0931:CABHMF>2.0.CO;2.

Wood, E. F., and Coauthors, 1998: The project for Intercomparison of Land-surface Parameterization Schemes (PILPS) Phase 2(c) Red–Arkansas River basin experiment: 1. Experiment description and summary intercomparisons. *Global Planet. Change*, **19**, 115–136, doi:10.1016/S0921-8181(98)00044-7.

Xue, M., K. K. Droegemeier, and V. Wong, 2000: The Advanced Regional Prediction System (ARPS): A multi-scale non-hydrostatic atmospheric simulation and prediction model. Part I: Model dynamics and verification. *Meteor. Atmos. Phys.*, **75**, 161–193, doi:10.1007/s007030070003.

Yamada, T. J., S. Kanae, T. Oki, and R. D. Koster, 2013: Seasonal variation of land–atmosphere coupling strength over the West African monsoon region in an atmospheric general circulation model. *Hydrol. Sci. J.*, **58**, 1276–1286, doi:10.1080/02626667.2013.814914.

Yucel, I., A. Onen, K. K. Yilmaz, and D. Gochis, 2015: Calibration and evaluation of a flood forecasting system: Utility of numerical weather prediction model, data assimilation and satellite-based rainfall. *J. Hydrol.*, **523**, 49–66, doi:10.1016/j.jhydrol.2015.01.042.